

Measurability of the tidal deformability by gravitational waves from coalescing binary neutron stars

Kenta Hotokezaka,¹ Koutarou Kyutoku,² Yu-ichiro Sekiguchi,³ and Masaru Shibata⁴

¹*Racah Institute of Physics, The Hebrew University of Jerusalem, Jerusalem 91904, Israel*

²*Interdisciplinary Theoretical Science (iTHES) Research Group, RIKEN, Wako, Saitama 351-0198, Japan*

³*Department of Physics, Toho University, Funabashi, Chiba 274-8510, Japan*

⁴*Yukawa Institute for Theoretical Physics, Kyoto University, Kyoto 606-8502, Japan*

(Received 22 November 2015; published 31 March 2016)

Combining new gravitational waveforms derived by long-term (14 to 16 orbit) numerical-relativity simulations with waveforms by an effective-one-body (EOB) formalism for coalescing binary neutron stars, we construct hybrid waveforms and estimate the measurability for the dimensionless tidal deformability of the neutron stars, Λ , by advanced gravitational-wave detectors. We focus on the equal-mass case with the total mass $2.7M_{\odot}$. We find that for an event at a hypothetical effective distance of $D_{\text{eff}} = 200$ Mpc, the distinguishable difference in the dimensionless tidal deformability will be ≈ 100 , 400, and 800 at 1σ , 2σ , and 3σ levels, respectively, for Advanced LIGO. If the true equation of state is stiff and the typical neutron-star radius is $R \gtrsim 13$ km, our analysis suggests that the radius will be constrained within ≈ 1 km at 2σ level for an event at $D_{\text{eff}} = 200$ Mpc. On the other hand, if the true equation of state is soft and the typical neutron-star radius is $R \lesssim 12$ km, it will be difficult to narrow down the equation of state among many soft ones, although it is still possible to discriminate the true one from stiff equations of state with $R \gtrsim 13$ km. We also find that gravitational waves from binary neutron stars will be distinguished from those from spinless binary black holes at more than 2σ level for an event at $D_{\text{eff}} = 200$ Mpc. The validity of the EOB formalism, Taylor-T4, and Taylor-F2 approximants as the inspiral waveform model is also examined.

DOI: [10.1103/PhysRevD.93.064082](https://doi.org/10.1103/PhysRevD.93.064082)

I. INTRODUCTION

The inspiral and the merger of coalescing compact binaries are the most promising sources for ground-based kilometer-size laser-interferometric gravitational-wave detectors [1–4]. Among them, Advanced LIGO started the first observational run from September 2015 [2] and has achieved the first direct detection of gravitational waves from the merger of a binary black hole [5]. We may expect that these gravitational-wave detectors will also detect the signals of gravitational waves from binary neutron-star mergers in a few years because the latest statistical studies suggest that these gravitational-wave detectors will observe gravitational waves from merger events as frequently as ~ 1 –100/yr if the designed sensitivity is achieved [6–8]. One of the primary purposes after the first detection of gravitational waves from binary neutron stars (and also a black-hole–neutron-star binary) will be to extract information of the neutron-star equation of state, which is still poorly constrained [9].

Extracting the *tidal deformability* of the neutron stars from gravitational waves emitted by binary-neutron-star inspirals is one of the most promising methods for constraining the neutron-star equation of state [10–21]. For this purpose, we need an accurate theoretical template of gravitational waves from binary neutron-star inspirals taking into account tidal-deformation effects that influence

the dynamics of the late inspiral orbits and modify the corresponding gravitational waveform. However, current post-Newtonian (PN) waveforms are not appropriate for the theoretical template, as Favata [18] and Yagi and Yunes [19] independently showed that uncertainties in the known PN waveforms can cause significant systematic errors in the tidal deformability estimates due to the unknown higher-order terms. In fact, Wade and his collaborators [20] evaluated the systematic errors using the waveforms derived from different PN families and confirmed that the estimated tidal deformability can be significantly biased. To derive an accurate theoretical template that is free from such uncertainties, high-accuracy numerical-relativity simulations are necessary. Several efforts for this purpose have been done recently [22–30].

In our previous paper [27], we reported our latest effort for deriving accurate gravitational waveforms from inspiraling binary neutron stars of typical mass ($1.35M_{\odot} - 1.35M_{\odot}$). We performed simulations for 15 to 16 inspiral orbits (30–32 wave cycles) up to the merger employing low-eccentricity initial data, then performed an extrapolation procedure with respect to the grid resolution, and finally derived waveforms with the total accumulated phase error within ~ 0.5 rad and amplitude error less than 2% to 3%. We then compared our numerical waveforms with the waveforms derived in an effective-one-body (EOB) formalism, developed by Bernuzzi, Nagar, and their

collaborators [28] (see also Refs. [15,31–35]). We have indicated that the EOB results agree well with the numerical-relativity results for a quite soft equation of state in which the neutron-star radius is small (~ 11 km), while for a stiff equation of state with a radius $\gtrsim 13.5$ km, a slight disagreement is present for the final inspiral stage just prior to the merger.

Combining numerical-relativity waveforms and resummed PN waveforms (by a Taylor-T4 approximant), Read and her collaborators constructed hybrid waveforms and analyzed the measurability of the tidal deformability for the first time [16]. The primary purpose of our paper is to quantitatively update their previous results by performing the same analysis as theirs using our new numerical waveforms. The motivation for this comes from the fact that the quality of our numerical waveforms is significantly improved: (i) the cycles of the new waveforms are double those of the waveforms previously used, (ii) the initial orbital eccentricity is reduced by more than an order of magnitude [36], and (iii) the convergence of the simulation results is much better and the numerical error is much lower than the previous results.

As a first step for constructing hybrid waveforms, we will compare new numerical gravitational waveforms for several equations of state (different from those employed in our previous papers) with the EOB waveforms, and we will reconfirm the conclusion in our previous paper [27]. Then, we will analyze the measurability of the tidal deformability using the new hybrid waveforms constructed by combining the numerical-relativity and EOB results. In this paper, we focus only on the measurability by ground-based advanced gravitational-wave detectors.

By comparing the hybrid waveforms derived from the numerical and EOB results with them, we also examine the validity of other analytic/semianalytic methods for modeling gravitational waveforms, paying special attention to Taylor-T4 (TT4) and Taylor-F2 (TF2) approximants in which the tidal correction is incorporated up to the first PN order (e.g., see Ref. [20]). We will indicate that the current version of these Taylor approximants does not yield waveforms as accurately as those by an EOB formalism for equal-mass binary neutron stars, primarily because of the lack of the higher-order PN terms.

The paper is organized as follows. In Sec. II, we briefly summarize the formulation and numerical schemes employed in our numerical-relativity study, and we also list the equations of state employed. In Sec. III, we present our new waveforms and compare them with those by the EOB and TT4 approximants. We then construct hybrid waveforms using the numerical and EOB waveforms. In Sec. IV, we explore the measurability of the tidal deformability using the hybrid waveforms. We also assess the validity of the EOB, TT4 (hybrid-TT4), and TF2 approximants for modeling inspiraling binary neutron stars. Section V is devoted to a summary. Throughout this paper, we employ the

geometrical units of $c = G = 1$ where c and G are the speed of light and the gravitational constant, respectively.

II. DERIVING NUMERICAL WAVEFORMS

We briefly summarize the formulation and numerical schemes of our numerical-relativity simulation, equations of state employed, and a method for deriving an extrapolated gravitational waveform from the raw numerical-relativity results.

A. Evolution and initial condition

We follow the inspiral, merger, and early stage of the postmerger of binary neutron stars using our numerical-relativity code, SACRA, whose details are described in Ref. [37]. As in our previous long-term simulations [27], we employ a moving puncture version of the Baumgarte-Shapiro-Shibata-Nakamura formalism [38], *locally* incorporating a Z4c-type constraint propagation prescription [39] (see Ref. [36] for our implementation) for a solution of Einstein's equation. SACRA implements a fourth-order finite differencing scheme in space and time with an adaptive mesh refinement (AMR) algorithm.

As in Ref. [27], we prepare nine refinement levels and 13 domains for the AMR algorithm. Each refinement domain consists of a uniform, vertex-centered Cartesian grid with $(2N + 1, 2N + 1, N + 1)$ grid points for (x, y, z) ; the equatorial plane symmetry at $z = 0$ is imposed. The half of the edge length of the largest domain (i.e., the distance from the origin to outer boundaries along each axis) is denoted by L , which is chosen to be larger than λ_0 , where $\lambda_0 = \pi/\Omega_0$ is the initial wavelength of the gravitational waves and Ω_0 is the initial orbital angular velocity. The grid spacing for each refinement level is $\Delta x_l = L/(2^l N)$, where $l = 0-8$. We denote Δx_8 by Δx in the following. In this work, we choose $N = 72, 60$, and 48 for examining the convergence properties of numerical results with respect to the grid resolution. With the highest grid resolution (for $N = 72$), the semimajor diameter of each neutron star is covered by about 120 grid points.

We prepare binary neutron stars in quasicircular orbits for the initial condition of the numerical simulations. The initial conditions are numerically obtained by using a spectral-method library, LORENE [40]. In this paper, we focus only on equal-mass systems with each neutron-star mass being $1.35M_\odot$. We follow 14–16 orbits in this study ($\approx 57-62$ ms duration for the last inspiral orbits). To do so, the orbital angular velocity of the initial configuration is chosen to be $m_0\Omega_0 \approx 0.0155$ ($f = \Omega_0/\pi \approx 371$ Hz for the total mass $m_0 = 2.7M_\odot$, where f denotes the gravitational-wave frequency). Some parameters for the models and settings for the simulations are listed in Table I.

For the computation of an accurate gravitational waveform in the numerical simulations, we have to employ

TABLE I. Equations of state (EOS) employed, the maximum mass of spherical neutron stars for given EOS, circumferential radius, dimensionless tidal deformability, and tidal Love number of $l = (2, 3, 4)$ for spherical neutron stars of mass $1.35M_\odot$, angular velocity of initial data, location of the outer boundaries along each axis, and the finest grid spacing in the three different resolution runs. m_0 denotes the total mass of the system for the infinite orbital separation. In this study, $m_0 = 2.7M_\odot$. For $m_0\Omega_0 \approx 0.0155$, the corresponding gravitational-wave frequency is ≈ 371 Hz.

EOS	$M_{\max}(M_\odot)$	$R_{1.35}$ (km)	Λ	$k_{2,1.35}$	$k_{3,1.35}$	$k_{4,1.35}$	$m_0\Omega_0$	L (km)	Δx (km)
APR4	2.20	11.09	322	0.0908	0.0234	0.00884	0.0156	2572	0.167, 0.209, 0.251
SFHo	2.06	11.91	420	0.0829	0.0216	0.00766	0.0155	2858	0.155, 0.186, 0.233
DD2	2.42	13.20	854	0.1007	0.0272	0.00996	0.0155	3258	0.177, 0.212, 0.265
TMA	2.02	13.85	1192	0.1103	0.0316	0.01229	0.0155	3430	0.186, 0.223, 0.279
TM1	2.21	14.48	1428	0.1059	0.0300	0.01154	0.0155	3644	0.198, 0.237, 0.297

initial data of a quasicircular orbit of negligible eccentricity. Such initial data are constructed by an eccentricity-reduction procedure described in Ref. [36]. For the initial data employed in this work, the residual eccentricity is $\lesssim 10^{-3}$.

B. Equation of state

We employ four tabulated equations of state for zero-temperature neutron-star matter derived recently by Hempel and his collaborators, and we refer to them as SFHo [41], DD2 [42], TMA [43], and TM1 [43]. Here, TM1 employed the same parameter set of a relativistic mean-field theory as that of one of Shen's equations of state [44]. All of these equations of state have been derived in relativistic mean-field theories. Some characteristic properties resulting from these equations of state are listed in Table I. For all of them, the predicted maximum mass for spherical neutron stars is larger than the largest well-measured mass of neutron stars, $\approx 2M_\odot$ [45]. The neutron-star radius with mass $1.35M_\odot$, $R_{1.35}$, is $\approx 11.9, 13.2, 13.9$ and 14.5 km for SFHo, DD2, TMA, and TM1; i.e., these are soft, moderately stiff, stiff, and very stiff equations of state, respectively.

In our previous works [25,27], we employed piecewise polytropic equations of state approximating tabulated equations of state. In this work, we employ the tabulated equations of state as they are to preserve the original form of each equation of state.

In the analysis for the measurability of the dimensionless tidal deformability, Λ , we also employ the numerical results for APR4 [46], for which a detailed numerical result was already reported in Ref. [27]. For this numerical simulation, we employed the piecewise polytropic approximation. $R_{1.35}$ for this equation of state is ≈ 11.1 km, and hence this equation of state is softer than SFHo, DD2, TMA, or TM1. As Table I shows, $R_{1.35}$ and Λ are systematically varied among the five equations of state employed. This is the reason that we pick up these equations of state in our present analysis for the measurability of Λ .

For the zero-temperature case, the thermodynamical quantities, i.e., the pressure, P , and the specific internal energy, ϵ , are written as functions of the rest-mass density, ρ . Here, the zero-temperature equations of state satisfy $d\epsilon = -Pd(1/\rho)$. In numerical simulations, we slightly

modify the original equations of state, adding a thermal part, to approximately take into account thermal effects, which play a role in the merger and postmerger phases. For this prescription, we use the same method as that used in our previous works (see, e.g., Refs. [27,47]).

C. Extraction of gravitational waves and extrapolation procedures

Gravitational waves are extracted from the outgoing component of the complex Weyl scalar Ψ_4 [37]. Ψ_4 can be expanded in the form

$$\Psi_4(t, r, \theta, \varphi) = \sum_{lm} \Psi_4^{l,m}(t, r) {}_{-2}Y_{lm}(\theta, \varphi), \quad (2.1)$$

where ${}_{-2}Y_{lm}(\theta, \varphi)$ denotes the spin-weighted spherical harmonics of weight -2 and $\Psi_4^{l,m}$ are expansion coefficients defined by this equation. In this work, we focus only on the $(l, |m|) = (2, 2)$ mode because we pay attention only to the equal-mass binary, and hence this quadrupole mode is the dominant one.

From the $(l, m) = (2, 2)$ mode, quadrupole gravitational waveforms are determined by

$$h_+(t, r) - ih_\times(t, r) = -\lim_{r \rightarrow \infty} \int^t dt' \int^t dt'' \Psi_4^{2,2}(t'', r), \quad (2.2)$$

where $h_+(t, r)$ and $h_\times(t, r)$ are the plus and cross modes of quadrupole gravitational waves, respectively (note that the waveforms h_+ and h_\times are actually derived by the integration method of Ref. [48]; see also Refs. [27,36]).

We evaluate Ψ_4 at a finite spherical-coordinate radius, $r \approx 200m_0$, following Ref. [27]. The waveforms are described as a function of the retarded time defined by

$$t_{\text{ret}} := t - r_*, \quad (2.3)$$

where r_* is the so-called tortoise coordinate defined by

$$r_* := r_A + 2m_0 \ln \left(\frac{r_A}{2m_0} - 1 \right), \quad (2.4)$$

with $r_A := \sqrt{A/4\pi}$ and A being the proper area of the extraction sphere. For simplicity, we define it by $r_A = r[1 + m_0/(2r)]^2$.

Since the waveform of $\Psi_4^{2,2}$, extracted at a finite radius, $r = r_0$, is systematically different from that at null infinity, we then compute an extrapolated waveform at $r_0 \rightarrow \infty$ using Nakano's method as [49,50]

$$\Psi_4^{l,m,\infty}(t_{\text{ret}}, r_0) = C(r_0) \left[\Psi_4^{l,m}(t_{\text{ret}}, r_0) - \frac{(l-1)(l+2)}{2r_A} \int^{t_{\text{ret}}} \Psi_4^{l,m}(t', r_0) dt' \right], \quad (2.5)$$

where $C(r_0) = 1 - 2m_0/r_A$, as described in Ref. [27].

As we have already mentioned, we always perform simulations for three different grid resolutions (with different values of the grid spacing Δx), and we obtain three waveforms of different accuracy determined by Δx . Then, we perform an extrapolation procedure for $\Delta x \rightarrow 0$ employing the same method as described in Ref. [27]. As in the previous results, we found that the convergence order is within 4 ± 1 irrespective of the equations of state employed.

It should be noted that the extrapolated numerical waveforms have the accumulated phase errors only within ~ 0.5 rad, as described in Ref. [27]. This value is much smaller than the phase differences among the different waveforms by different modeling (see Sec. IV B). Therefore, we expect that the numerical errors in our extrapolated

waveforms do not significantly change our results for the analysis of the measurability described in Sec. IV.

III. CONSTRUCTING A HYBRID WAVEFORM

Because we follow only 14–16 inspiral orbits, only gravitational waveforms with $f \gtrsim 370$ Hz can be derived. For exploring the measurability of the tidal deformability, such waveforms are not well suited. To supplement the earlier waveform for $f < 370$ Hz, we consider hybridization between the numerical waveform and a waveform derived by an analytic/semianalytic calculation, by which the waveform for the lower-frequency band is filled up.

For the hybridization, we first have to align the time and phase of the numerical-relativity waveform, h_{NR} , and a waveform by an analytic/semianalytic formulation, h_{SA} . Here, complex waveforms $h(t)$ are defined by $h_+(t) - ih_\times(t)$, with $h_+(t)$ and $h_\times(t)$ representing the plus and cross modes, respectively. We then calculate

$$I(\tau, \phi) = \int_{t_i}^{t_f} dt |h_{\text{NR}}(t) - h_{\text{SA}}(t + \tau) e^{i\phi}|^2 \quad (3.1)$$

and search for τ 's and ϕ 's that minimize I . Here, t in this section always denotes the retarded time, t_{ret} , and we choose $t_i = 5$ ms and $t_f = 20$ ms, as in our previous paper [27]. At $t = 5$ ms and 20 ms, the gravitational-wave frequency is $f \approx 380$ Hz and 420 Hz, respectively (see Fig. 7 in Appendix A), and the number of the wave cycle in this duration is ~ 6 (see Fig. 1). We choose this window because we would like to employ the time for it as early as

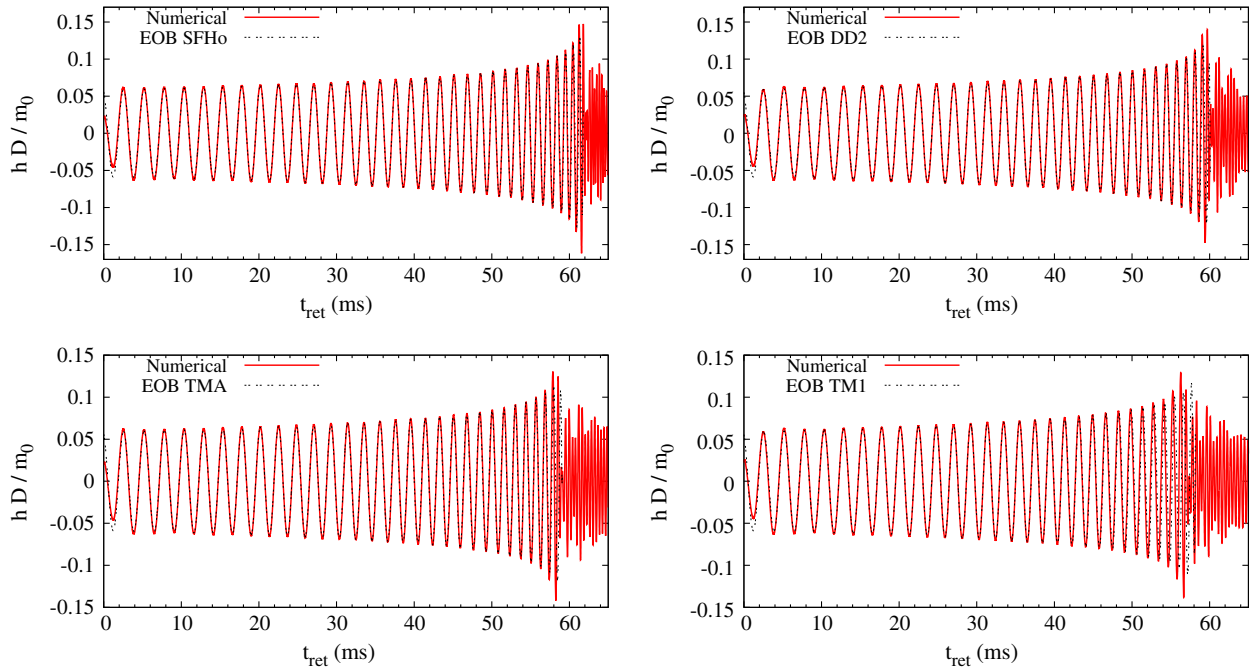


FIG. 1. Comparison of numerical (solid curves) and EOB (dot-dot curves) waveforms for the late inspiral phase. The upper left, upper right, lower left, and lower right panels show the results for SFHo, DD2, TMA, and TM1, respectively. Gravitational waves (plus mode) observed along the rotational axis (perpendicular to the orbital plane) are shown. D denotes the distance from the source to the observer.

possible. Here, for the first ≈ 5 ms just after the simulations started, the waveforms have unphysical modulation, and hence we choose 5 ms for t_i . 20 ms for t_f is rather *ad hoc*. To check that our conclusion for the measurability of the tidal deformability does not depend strongly on the choice of t_i and t_f , we also construct other hybrid waveforms, choosing $t_i = 10$ ms and $t_f = 25$ ms ($f \approx 390$ and 430 Hz, respectively), and use them for calibrating the results in Sec. IV A.

For the values of τ and ϕ that we determine, we construct a hybrid waveform. Following Refs. [27,51], we define the hybrid waveform by

$$h_{\text{hyb}}(t) = \begin{cases} h_{\text{SA}}(t')e^{i\phi} & t \leq t_i, \\ h_{\text{NR}}(t)H(t) + h_{\text{SA}}(t')e^{i\phi}[1 - H(t)] & t_i \leq t \leq t_f, \\ h_{\text{NR}}(t) & t \geq t_f, \end{cases} \quad (3.2)$$

where $t' = t + \tau$, and we choose a Hann window function for $H(t)$ as

$$H(t) := \frac{1}{2} \left[1 - \cos \left(\pi \frac{t - t_i}{t_f - t_i} \right) \right]. \quad (3.3)$$

Figure 1 plots the extrapolated numerical waveforms and waveforms by an EOB formalism [29] for four different equations of state (see Fig. 3 and Appendix A of Ref. [27] for the waveform with APR4 and the EOB formalism that we employ in this work, respectively). For these plots, we align the numerical and EOB waveforms in the same way as the hybrid construction. It is found that the two waveforms agree well with each other in their early part, i.e., for $t_{\text{ret}} \lesssim 45$ ms (for the first ~ 20 wave cycles). In particular, the phases for the two waveforms agree with each other with the disagreement of order 0.01 rad for this stage, as we demonstrated in our previous work [27]. This suggests that our hybridization would work well whenever we employ the EOB waveforms, irrespective of the choice of (t_i, t_f) , as long as they are sufficiently small, $\ll 45$ ms. We estimate a degree of the disagreement in the matching window by

$$\left[\frac{\min_{\tau, \phi} I(\tau, \phi)}{\int_{t_i}^{t_f} dt \{ |h_{\text{NR}}(t)|^2 + |h_{\text{SA}}(t)|^2 \}} \right]^{1/2}, \quad (3.4)$$

and it is always as small as $\lesssim 2 \times 10^{-2}$. This error comes primarily from the error in amplitude of the numerical waveforms because the estimated maximum error size is 2%–3% in the amplitude. On the other hand, the phase error has a minor contribution for this error.

The numerical and EOB waveforms agree reasonably well with each other even in the late inspiral phase, up to a few wave cycles prior to the merger (see also Fig. 7 in Appendix A for supplementary information). This indicates that the tidal-deformation effects would be fairly well taken into account in the employed EOB formalism, as we

already mentioned in Ref. [27]. Because of these reasons, we construct hybrid waveforms employing the EOB waveforms as h_{SA} and use them for analyzing the measurability of the tidal deformability.

We note that for stiff equations of state like TMA and TM1 for which the dimensionless tidal deformability is larger than 1000, the disagreement between the numerical and EOB waveforms is appreciable for the last few wave cycles, as was already pointed out in Ref. [27]. This suggests that there is still room for incorporating additional tidal effects into the EOB formalism [52]. On the other hand, for softer equations of state with $\Lambda < 1000$, the disagreement is minor. This indicates that the EOB waveforms well capture the tidal-deformation effects, as long as $\Lambda \ll 1000$.

We also perform the hybridization employing the TT4 waveforms [53,54] incorporating the tidal effects up to the first PN (1PN) order [14]. In the TT4 approximant, the evolution of the gravitational-wave frequency is determined by (see, e.g., Ref. [20])

$$\begin{aligned} \frac{dx}{dt} = & \frac{16}{5m_0} x^5 \left[1 - \frac{487}{168} x + 4\pi x^{3/2} + \frac{274229}{72576} x^2 - \frac{254}{21} \pi x^{5/2} \right. \\ & + \left(\frac{178384023737}{3353011200} + \frac{1475\pi^2}{192} - \frac{1712}{105} \gamma_E \right. \\ & \left. \left. - \frac{856}{105} \ln(16x) \right) x^3 + \frac{3310}{189} \pi x^{7/2} \right. \\ & \left. + \frac{39}{8} \Lambda x^5 + \frac{5203}{896} \Lambda x^6 \right], \end{aligned} \quad (3.5)$$

where $x(t) := [\pi m_0 f(t)]^{2/3}$ and γ_E is Euler's constant. We assume that the quadrupole-wave amplitude is determined by Eq. (71) of Ref. [55]. Here, for simplicity, we restrict our attention only to the equal-mass case, and in addition, we do not take into account the effect of the tidal deformability in the amplitude because it plays only a minor role for analyzing the measurability [32].

After the alignment procedure for time and phase, we also compare the numerical waveforms with the TT4 waveforms. Figure 2 shows the results for the same comparison as in Fig. 1. This shows that the agreement between the numerical and TT4 waveforms is worse than that between the numerical and EOB waveforms. Specifically, the phase evolution in the TT4 approximant is slower than that in the EOB formalism. We note that the tidal effects accelerate the orbital evolution in the late inspiral phase because the tidal force strengthens the attractive force between two neutron stars for such orbits. Thus, we conclude that the tidal effects are underestimated in the employed TT4 approximant. This should be the case not only for the very late inspiral phase but also for the earlier inspiral phase. An analysis of the gravitational-wave phase evolution indicates that this would be due to the lack of the higher-order PN terms of order $O(x^{13/2})$ or more: terms with more than 1.5PN order with respect to the

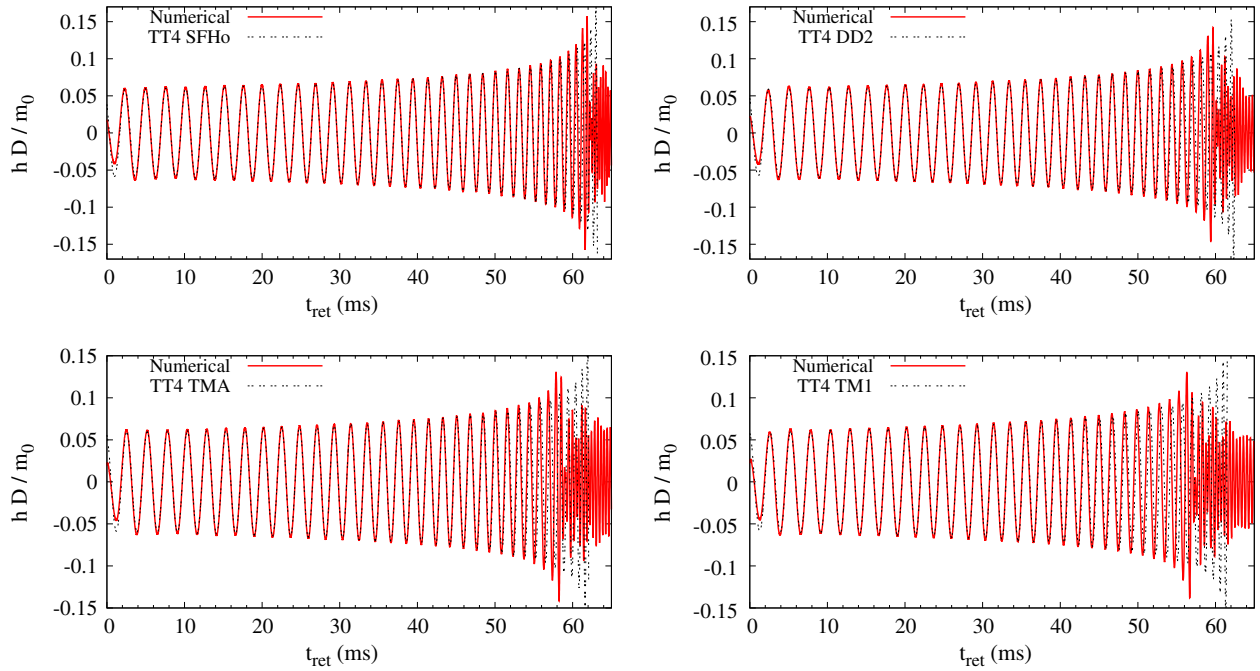


FIG. 2. The same as Fig. 1, but for the case that TT4 waveforms are used for the comparison with the numerical waveforms.

leading-order tidal-deformation effect. We provide evidence for this in Appendix B. For this reason, we suppose that the EOB formalism could give a better waveform than the TT4 formalism.

Figure 3 plots the Fourier spectra of the hybrid waveforms (numerical plus EOB waveforms) together with a designed noise curve of Advanced LIGO, $S_n^{1/2}$ (for the zero detuning high power configuration) [56] and with the spectrum of a binary-black-hole merger of mass $1.35M_\odot - 1.35M_\odot$. Here, $S_n(f)$ denotes the one-sided noise spectrum density of gravitational-wave detectors. The numerical waveform for the binary black hole is taken from the SXS Gravitational Waveform Database [57], and we employ SXS:BBH:001. In this paper, the Fourier transform is defined by

$$\tilde{h}(f) := \int dt h_+(t) \exp(-2\pi i f t), \quad (3.6)$$

where $h_+(t)$ denotes the plus-mode gravitational waveform. For binary neutron stars, the overall shape of $h_\times(t)$ is approximately the same as that of $h_+(t)$ except for a $\pi/2$ phase difference, and hence, the Fourier transformation of the cross mode, $h_\times(t)$, results approximately in $-i\tilde{h}(f)$.

The response of gravitational-wave detectors for a gravitational-wave event of coalescing binary neutron stars is written in the form

$$\bar{h}(t) = H_+(\theta, \varphi, \iota, \psi_p) h_+(t) + H_\times(\theta, \varphi, \iota, \psi_p) h_\times(t), \quad (3.7)$$

where H_+ and H_\times are functions of the source angular direction denoted by (θ, φ) , of the inclination angle of the binary orbital plane with respect to the line of the sight to the source denoted by ι , and of the polarization angle

denoted by ψ_p . Thus, the Fourier transformation of $\bar{h}(t)$ is written as

$$\bar{h}(f) \approx H(\theta, \varphi, \iota, \psi_p) \tilde{h}(f), \quad (3.8)$$

where $H = H_+ - iH_\times$, for which $|H| \leq 1$. Taking into account this form, we define the effective distance to the

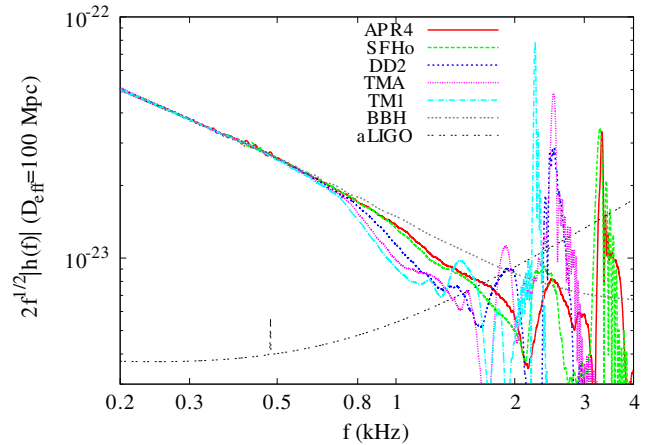


FIG. 3. Fourier spectra of the hybrid waveforms for five different equations of state for a hypothetical effective distance of $D_{\text{eff}} = 100$ Mpc. The dot-dot curve for Advanced LIGO (referred to as aLIGO) denotes $S_n^{1/2}$. Here, S_n is the one-sided noise spectrum density for the “zero detuning high power” configuration [56]. The dot-dot-dot curve denotes the Fourier spectrum for a spinless binary black hole of mass $1.35M_\odot - 1.35M_\odot$ (plotted only for $f \geq 375$ Hz). To find the approximate SNR, the spectrum is shown with an additional factor of 2; see Eq. (3.9).

source by $D_{\text{eff}} := D|H|^{-1}$, where D is the proper distance to the source. In the following, we always refer to D_{eff} (not D) as the effective distance to the source, and we typically consider an event at $D_{\text{eff}} = 200$ Mpc. This is equivalent to an event at a distance of 200 Mpc with the optimal orientation and sky location. The reason for this choice is that statistical studies have predicted typically ~ 1 detection per year for $D_{\text{eff}} \lesssim 200$ Mpc [58].

Figure 3 clearly shows that the difference in the Fourier spectra among the waveforms of different equations of state becomes appreciable for $f \gtrsim 500$ Hz. In particular, for $f \gtrsim 700$ Hz, the difference is remarkable. This stems primarily from the difference in the tidal deformability. For larger values of Λ , the spectrum amplitude decreases more steeply for $f \gtrsim 700$ Hz because the binary orbit is evolved faster. Here, we note that (i) the late inspiral waveform determines the spectrum only for $f \lesssim 1$ kHz, (ii) the final-inspiral to merger waveform determines the spectrum approximately for $1 \text{ kHz} \lesssim f \lesssim 2 \text{ kHz}$, and (iii) several bumps and peaks for $f \gtrsim 2$ kHz are determined by the postmerger waveform (i.e., by gravitational waves from remnant massive neutron stars formed after the merger). It should also be noted that the noise amplitude of the gravitational-wave detectors monotonically increases for $f \gtrsim 500$ Hz. This indicates that the equation of state (tidal deformability) could be constrained primarily by analyzing the spectrum in the late inspiral and merger waveforms and that the tidal deformability could be more accurately measured for stiffer equations of state of a larger value of Λ .

We briefly comment on the strength of gravitational waves found for 2–3.5 kHz as peaks of the Fourier spectrum, which are emitted from the massive neutron stars formed in the postmerger phase (see, e.g., Ref. [47]). To assess the *detectability* for them, we estimate the signal-to-noise ratio defined by

$$\text{SNR} = \left[4 \int_{f_i}^{f_f} \frac{|\tilde{h}(f)|^2}{S_n(f)} df \right]^{1/2}. \quad (3.9)$$

For evaluating the strength of the peaks, we choose $f_i = 2$ kHz and $f_f = 4$ kHz and the one-sided noise spectrum density for the zero detuning high power configuration of Advanced LIGO as $S_n(f)$ [56]. It is found that the SNR is 0.5–0.9 for $D_{\text{eff}} = 200$ Mpc. For stiffer equations of state, this value is larger (0.5, 0.6, 0.7, 0.9, and 0.9 for APR4, SFHo, DD2, TMA, and TM1). Since a $\text{SNR} \gtrsim 5$ would be required for the confirmed detection (due to the presence of the Gaussian and other noises in the detectors; see, e.g., Ref. [59]), this peak will be detected with a high confidence level only for a nearby event with $D_{\text{eff}} \lesssim 20 - 35$ Mpc for the Advanced LIGO-class detectors, even if perfect templates for this waveform could be prepared. We note that for a gravitational-wave event of an equal-mass binary neutron star with $m_0 = 2.7M_\odot$ and $D_{\text{eff}} = 200$ Mpc, the total signal-to-noise ratio for the entire inspiral phase will be

≈ 17 (for a choice of $f_i < 10$ Hz and $f_f > 2$ kHz) irrespective of the equations of state employed. Therefore, the expected SNR for the kilohertz peaks is much lower than the SNR for the inspiral signal for the Advanced LIGO-class detectors. This motivates us to focus primarily on the late inspiral phase for extracting the information of the neutron-star equation of state—at least in the near future. (Of course, we will be more optimistic about the detectability of this peak with more sensitive gravitational-wave detectors in the future.)

IV. MEASURABILITY OF THE TIDAL DEFORMABILITY

Following Ref. [16], we define a measure of the distinguishability of two waveforms by

$$\|h_1 - h_2\|^2 := \min_{\Delta t, \Delta \phi} \left[4 \int_{f_i}^{f_f} \frac{|\tilde{h}_1(f) - \tilde{h}_2(f) e^{i(2\pi f \Delta t + \Delta \phi)}|^2}{S_n(f)} df \right], \quad (4.1)$$

where $\tilde{h}_1(f)$ and $\tilde{h}_2(f)$ are the Fourier transform of the waveforms $h_1(t)$ and $h_2(t)$. f_i and f_f are carefully chosen later for the analysis of the measurability. In the following, we always employ the one-sided noise spectrum density for the zero detuning high power configuration of Advanced LIGO as $S_n(f)$ [56].

As was shown in Ref. [60], $\|h_1 - h_2\| = 1$ corresponds to a 1σ error in parameter estimation, and hence two waveforms h_1 and h_2 are said to be marginally distinguishable if $\|h_1 - h_2\| = 1$. Thus, we assess the measurability of the tidal deformability by calculating $\|h_1 - h_2\|$ for a variety of waveform combinations.

In the calculation of $\|h_1 - h_2\|$, it is ideal to choose $f_i < 10$ Hz and $f_f > 4$ kHz. Computationally, choosing $f_f > 4$ kHz does not matter, whereas choosing the low value of f_i is expensive because the data size for the waveforms increases approximately as $f_i^{-8/3}$. Here, we should keep in mind that the noise amplitude of ground-based gravitational-wave detectors steeply increases with the decrease of the frequency for $f < 50$ Hz toward 10 Hz. Hence, it is practically possible to obtain an approximate result for $\|h_1 - h_2\|$, even if we choose a value of f_i that is larger than 10 Hz. Thus, as a first step, we calibrated how high a value of f_i would be acceptable by analyzing $\|h_1 - h_2\|$ by using a TF2 approximant for \tilde{h}_1 and \tilde{h}_2 . Here, the amplitude and the phase of the TF2 approximant are calculated by using a stationary phase approximation and the results are written simply in a polynomial form with respect to $(\pi m_0 f)^{2/3}$ [54] (see also Appendix C). In the present analysis, the tidal effect is incorporated up to the 1PN order as in the TT4 case.

It is found (see Appendix C for the results) that for $f_i = 30$ and 50 Hz, the results for $\|h_1 - h_2\|$ are not significantly different from that for $f_i = 10$ Hz: the values of $\|h_1 - h_2\|$ are systematically underestimated by $\approx 5\%$ and 15% for

TABLE II. $\|h_1 - h_2\|$ for a combination of hybrid waveforms with different equations of state for an event of $D_{\text{eff}} = 200$ Mpc for which the total SNR would be ≈ 17 for our choice of S_n (for $f_i \lesssim 10$ Hz and $f_f \gtrsim 4$ kHz). The left and right tables show the results for $f_i = 30$ and 50 Hz, respectively. For the top, second, and third tables, $f_f = 1, 2,$ and 4 kHz, respectively. Note that the listed values are proportional to $200 \text{ Mpc}/D_{\text{eff}}$ and, for $f_i = 30$ and 50 Hz, the values for a given combination of two waveforms would be smaller than those for $f_i = 10$ Hz by $\approx 5\%$ and 15% , respectively (see Appendix C).

0.03–1 kHz	APR4	SFHo	DD2	TMA	TM1	0.05–1 kHz	APR4	SFHo	DD2	TMA	TM1
APR4	...	0.4	2.2	2.9	3.4	APR4	...	0.3	2.0	2.7	3.1
SFHo	0.4	...	1.9	2.7	3.2	SFHo	0.3	...	1.7	2.5	3.0
DD2	2.2	1.9	...	1.3	2.4	DD2	2.0	1.7	...	1.2	2.3
TMA	3.2	2.7	1.3	...	1.6	TMA	2.7	2.5	1.2	...	1.5
TM1	3.4	3.2	2.4	1.6	...	TM1	3.1	3.0	2.3	1.5	...
0.03–2 kHz	APR4	SFHo	DD2	TMA	TM1	0.05–2 kHz	APR4	SFHo	DD2	TMA	TM1
APR4	...	0.7	2.3	3.0	3.5	APR4	...	0.6	2.2	2.8	3.2
SFHo	0.7	...	2.1	2.8	3.3	SFHo	0.6	...	1.9	2.6	3.1
DD2	2.3	2.1	...	1.6	2.5	DD2	2.2	1.9	...	1.5	2.4
TMA	3.0	2.8	1.6	...	1.7	TMA	2.8	2.6	1.5	...	1.7
TM1	3.5	3.3	2.5	1.7	...	TM1	3.2	3.1	2.4	1.7	...
0.03–4 kHz	APR4	SFHo	DD2	TMA	TM1	0.05–4 kHz	APR4	SFHo	DD2	TMA	TM1
APR4	...	0.8	2.4	3.0	3.5	APR4	...	0.8	2.2	2.8	3.3
SFHo	0.8	...	2.1	2.8	3.3	SFHo	0.8	...	2.0	2.6	3.1
DD2	2.4	2.1	...	1.7	2.6	DD2	2.2	2.0	...	1.6	2.4
TMA	3.0	2.8	1.7	...	1.9	TMA	2.8	2.6	1.6	...	1.8
TM1	3.5	3.3	2.6	1.9	...	TM1	3.3	3.1	2.4	1.8	...

$f_i = 30$ and 50 Hz, respectively; see Appendix C. For $f_i = 100$ Hz, the values of $\|h_1 - h_2\|$ are underestimated by up to $\sim 30\%$. [We note that for $f_i = 10, 30, 50,$ and 100 Hz with $f_f = 4$ kHz, the SNR of Eq. (3.9) is $\approx 17, 16, 13,$ and 9 for $D_{\text{eff}} = 200$ Mpc.] Thus, in this paper, we employ $f_i = 30$ Hz for the analysis of the measurability of the tidal deformability performed in Sec. IV A and $f_i = 50$ Hz for the calibration of the several model waveforms (see Sec. IV B).

For f_f , we choose 1, 2, and 4 kHz. As we have already mentioned, the contribution to the SNR from $f \geq 2$ kHz is minor, and hence the results for $\|h_1 - h_2\|$ with $f_i = 2$ and 4 kHz are approximately identical (see Sec. IV A and Appendix C).

A. Analysis with the hybrid waveforms

Table II lists the values of $\|h_1 - h_2\|$ for all of the combination of the hybrid waveforms with the five equations of state for an event of $D_{\text{eff}} = 200$ Mpc. Figure 4 also plots $\|h_1 - h_2\|$ as a function of $\delta\Lambda = |\Lambda_1 - \Lambda_2|$ for $f_i = 30$ or 50 Hz and $f_f = 4$ kHz. Here, $\delta\Lambda$ denotes the absolute value in the difference of the dimensionless tidal deformability of two different equations of state. Table II shows that the values of $\|h_1 - h_2\|$ depend very weakly on the value of f_f , as long as it is larger than 2 kHz. Furthermore, for $f_f = 2$ and 4 kHz, the values of $\|h_1 - h_2\|$ are only slightly [by $(0.1-0.4) \times (D_{\text{eff}}/200 \text{ Mpc})^{-1}$] larger than

those for $f_f = 1$ kHz. It is also found that the difference is large for the combination of two soft equations of state. All of these results agree totally with the results in Appendix C, and hence we may conclude that they hold universally irrespective of the model waveforms. From these results, we confirm that the measurability is determined primarily by the late inspiral waveform, and the contribution of the merger and postmerger waveforms is minor.

Table II also shows that, for a given combination of two waveforms, the values for $f_i = 50$ Hz are by $\sim 10\%$ smaller than those for $f_i = 30$ Hz. This also agrees quantitatively with the results in the analysis in terms of the Taylor-F2 approximant (see Appendix C), and hence we could suppose that the values of $\|h_1 - h_2\|$ for $f_i = 30$ Hz would be smaller by only $\sim 5\%$ than those for $f_i = 10$ Hz. Nevertheless, they depend slightly on the value of f_i . This implies that the measurability of the tidal effect is determined not only by the late inspiral waveform but also by the relatively early one.

We also calculated $\|h_1 - h_2\|$ using other hybrid waveforms derived with $(t_i, t_f) = (10, 25 \text{ ms})$; see Eq. (3.1). We confirmed that the results depend only weakly on the choice of t_i and t_f . Specifically, the change in the values of $\|h_1 - h_2\|$ shown in Table II is within 0.1, irrespective of the waveforms.

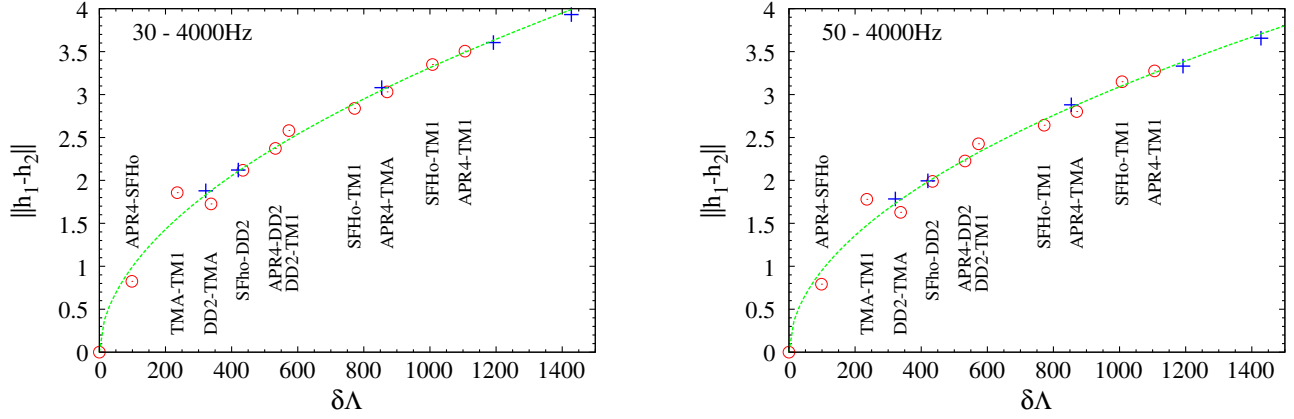


FIG. 4. $\|h_1 - h_2\|$ for the hybrid waveforms as a function of $\delta\Lambda = |\Lambda_1 - \Lambda_2|$, with $D_{\text{eff}} = 200$ Mpc (the open circles). The left and right panels show results for $(f_i, f_f) = (30 \text{ Hz}, 4 \text{ kHz})$ and $(50 \text{ Hz}, 4 \text{ kHz})$, respectively. The values of $\|h_1 - h_2\|$ are proportional to $200 \text{ Mpc}/D_{\text{eff}}$. The dashed curve in each plot is a fitting formula in the form $\|h_1 - h_2\| = A(\delta\Lambda/1000)^b$, where $(A, b) = (3.31, 0.522)$ and $(3.09, 0.511)$ for the left and right panels, respectively. The labels like APR4-SFHo show the combination of two equations of state for each value of $\delta\Lambda$. The crosses denote the results of $\|h_1 - h_2\|$ for the combination of binary neutron stars and binary black holes of mass $1.35M_\odot - 1.35M_\odot$.

Figure 4 shows that for $\delta\Lambda \gtrsim 100, 400, \text{ and } 800$, $\|h_1 - h_2\|$ is larger than 1, 2, and 3, respectively, for $D_{\text{eff}} = 200$ Mpc (note that if $f_i = 10$ Hz, the values of $\|h_1 - h_2\|$ would be by $\sim 5\%$ and 15% larger than those for $f_i = 30$ and 50 Hz, respectively; see Appendix C). This implies that, for an event of $D_{\text{eff}} = 200$ Mpc, two equations of state are marginally distinguishable by the observation of inspiral and merger waveforms by advanced gravitational-wave detectors if $\delta\Lambda \gtrsim 100$.

The neutron-star radius increases approximately monotonically with Λ . For the five equations of state employed in this paper, the radius of $1.35M_\odot$ neutron stars is written as

$$R_{1.35} = (13.565 \pm 0.076) \text{ km} \left(\frac{\Lambda}{1000} \right)^{0.16735 \pm 0.0094}, \quad (4.2)$$

where the standard errors shown for this fitting formula are at 1σ level. By taking the variation, the relative difference in the radius, $\delta R_{1.35}$, is related to $\delta\Lambda$ by

$$\delta R_{1.35} = (0.91 \pm 0.05) \text{ km} \left(\frac{R_{1.35}}{13 \text{ km}} \right) \left(\frac{\delta\Lambda}{400} \right) \left(\frac{\Lambda}{1000} \right)^{-1}. \quad (4.3)$$

For stiff equations of state that yield a large neutron-star radius of $R_{1.35} \gtrsim 13.5$ km, i.e., $\Lambda \gtrsim 1000$, the $\delta\Lambda$'s for two different equations of state can become larger than ~ 400 if the difference in $R_{1.35}$ is larger than ≈ 0.9 km. Thus, if the true equation of state is stiff, the equation of state will be strongly constrained for an event of the advanced detectors at $D_{\text{eff}} \lesssim 200$ Mpc, by which the measurability of $\delta\Lambda$ is ≈ 400 at the 2σ level.

By contrast, among soft equations of state, the difference in Λ is not as large as 400 (for the typical neutron-star mass $1.30M_\odot - 1.40M_\odot$). For example, $\delta\Lambda$ for the APR4 and SFHo equations of state is ~ 100 , although the difference in

radius is ≈ 0.8 km for neutron stars of mass $1.35M_\odot$ in these equations of state. This implies that it will not be easy to accurately identify the true equation of state among many candidate soft equations of state for a typical Advanced LIGO event at $D_{\text{eff}} = 200$ Mpc. The reason for this is quite simple: the phase difference between two waveforms for two different soft equations of state is appreciable only for a high-frequency range of $\gtrsim 1$ kHz, for which the sensitivity of the operating and planned gravitational-wave detectors is not very high (see Fig. 3). This situation cannot be significantly improved even if we take into account the merger and postmerger waveforms, because gravitational waves in these phases have a high frequency, and they do not contribute a lot to enhancing the signal-to-noise ratio, as shown in Table II. However, even if the true equation of state is soft, it will still be possible to discriminate it from stiff equations of state that yield $\Lambda \gtrsim 1000$. Thus, the detection of gravitational waves emitted at $D_{\text{eff}} \lesssim 200$ Mpc for the advanced detectors will give us an impact even if the true equation of state is soft. We also should mention that if, fortunately, we have a nearby event at $D_{\text{eff}} \ll 200$ Mpc, the outlook will become much more optimistic.

Next, we evaluate $\|h_1 - h_2\|$ by employing hybrid waveforms for binary neutron stars and spinless binary black holes of mass $1.35M_\odot - 1.35M_\odot$, assuming $D_{\text{eff}} = 200$ Mpc. For this analysis, a hybrid waveform for the binary black hole is constructed by combining a numerical waveform and an EOB one, as we already did for binary neutron stars. Here, the numerical waveform is again taken from the SXS Gravitational Waveform Database [57] and we employ SXS:BBH:001. Table III lists the results of $\|h_1 - h_2\|$ and, in Fig. 4, we plot the data setting $\Lambda = 0$ for the black-hole case (see the crosses). These show that $\|h_1 - h_2\| \gtrsim 2$ for $D_{\text{eff}} = 200$ Mpc, irrespective of which

TABLE III. The same as Table II but in between the hybrid waveforms for binary neutron stars and binary black holes.

	APR4	SFHo	DD2	TMA	TM1
0.03–1 kHz	1.4	1.8	2.9	3.4	3.8
0.03–2 kHz	1.9	2.1	3.1	3.6	3.9
0.03–4 kHz	1.9	2.1	3.1	3.6	3.9
0.05–1 kHz	1.3	1.6	2.7	3.2	3.5
0.05–2 kHz	1.8	1.9	2.8	3.3	3.6
0.05–4 kHz	1.8	2.0	2.9	3.3	3.7

neutron-star equations of state we employ. This indicates that gravitational waves from binary neutron stars for $D_{\text{eff}} \lesssim 200$ Mpc will be distinguished from those from binary black holes of the same mass with a certain confidence level.

Figure 4 also shows that the relation between $\|h_1 - h_2\|$ and $\delta\Lambda$, satisfied for binary neutron stars, is approximately satisfied even for the waveform combination of binary neutron stars and binary black holes. This also indicates that gravitational waves from binary neutron stars for $D_{\text{eff}} \lesssim 200$ Mpc will be distinguished from those from binary black holes at the 2σ level if the value of Λ for the neutron stars is larger than ~ 400 .

Before closing this subsection, we note the following point. By comparing our results with those in Ref. [16], it is found that our results for the measurability of $\delta\Lambda$ and $R_{1.35}$ agree approximately with theirs. However, this is accidental. In Ref. [16], the measurability was explored by choosing f_i in Eq. (4.1) to be 200 Hz, while we choose it to be 30 Hz. As we found in Table II (see also Appendix C), the values of $\|h_1 - h_2\|$ systematically decrease with the increase of f_i for a given value of f_f . We checked that for $f_i = 200$ Hz, the values of $\|h_1 - h_2\|$ could be half of those for $f_i = 30$ Hz. This implies that our results, based on new hybrid waveforms, actually show weaker measurability than those in Ref. [16]. The precise reason is not very clear. However, it is reasonable to speculate that, in the previous work, the numerical dissipation and the absence of any appropriate extrapolation procedure result in a spuriously shorter merger time, even for the highest-resolution runs, as shown in Refs. [27,47], so that the tidal effects could be spuriously overestimated. In addition, as noted in Ref. [16], the systematic error in their hybrid waveforms might be non-negligible because of a small number of the wave cycles and large initial residual eccentricity. These errors would also systematically enhance the measurability of the tidal deformability of Ref. [16].

B. Validity of analytic/semianalytic waveforms

We then evaluate $\|h_1 - h_2\|$ by choosing the hybrid waveforms to be h_1 , while the EOB, hybrid-TT4, and TF2 waveforms are h_2 . Here, as the EOB waveforms, we only take into account the inspiral part. Note that in the EOB

formalism we employ in this paper, the amplitude approaches zero if the orbital separation approaches zero. The ‘‘hybrid-TT4’’ waveforms are constructed by combining the numerical and TT4 waveforms, and the Fourier transformation is then performed straightforwardly. The TF2 approximant that we employ in this paper is described in Appendix C.

The purpose of this analysis is to assess how appropriate the EOB/hybrid-TT4/TF2 waveforms are as *inspiral* model gravitational waveforms. We note that for the EOB and TF2 waveforms employed, the spectrum with $f \gtrsim 1$ kHz is not very realistic because of the absence of the merger and postmerger waveforms, and hence it is not appropriate to take the higher-frequency part into consideration for the comparison with the hybrid waveforms. Also, as we have already shown in Sec. IV A, the values of $\|h_1 - h_2\|$ for $(f_i, f_f) = (50 \text{ Hz}, 1 \text{ kHz})$ are only smaller by ~ 0.2 than those for $(f_i, f_f) = (30 \text{ Hz}, 1 \text{ kHz})$ for an event of Advanced LIGO at $D_{\text{eff}} = 200$ Mpc. Thus, in this section, all the analyses will be performed choosing $(f_i, f_f) = (50 \text{ Hz}, 1 \text{ kHz})$ for simplicity.

Three panels of Table IV list the values of $\|h_1 - h_2\|$ for $f_i = 50$ Hz and $f_f = 1$ kHz for the combination of the hybrid and other waveforms assuming $D_{\text{eff}} = 200$ Mpc. From the comparison between Tables II and IV, it is found that for the APR4, SFHo, DD2, and TMA equations of state, the EOB waveforms can reproduce approximately the same results of $\|h_1 - h_2\|$ (within the error of ± 0.2) as for the hybrid (hybrid-EOB) waveforms. This fact makes us confirm again that the EOB formalism would have already become robust for generating accurate inspiral waveform

 TABLE IV. The same as Table II but between the hybrid and EOB waveforms (1st-5th rows), between the hybrid and hybrid-TT4 waveforms (6th-10th rows), and between the hybrid and TF2 waveforms (11th-15th row). $f_i = 50$ Hz and $f_f = 1$ kHz are chosen.

0.05–1 kHz	APR4	SFHo	DD2	TMA	TM1
EOB:APR4	0.2	0.3	1.9	2.6	3.1
EOB:SFHo	0.5	0.2	1.6	2.4	2.9
EOB:DD2	2.0	1.7	0.2	1.3	2.2
EOB:TMA	2.8	2.6	1.2	0.3	1.5
EOB:TM1	3.1	3.0	2.0	0.9	0.9
hybrid-TT4:APR4	0.2	0.5	2.1	2.7	3.2
hybrid-TT4:SFHo	0.2	0.2	1.9	2.6	3.0
hybrid-TT4:DD2	1.7	1.4	0.4	1.5	2.5
hybrid-TT4:TMA	2.3	2.1	0.7	0.6	1.9
hybrid-TT4:TM1	2.8	2.6	1.8	1.0	0.7
TF2:APR4	0.3	0.4	2.1	2.7	3.2
TF2:SFHo	0.4	0.3	1.8	2.5	3.1
TF2:DD2	1.9	1.6	0.4	1.5	2.4
TF2:TMA	2.7	2.5	1.0	0.5	1.7
TF2:TM1	3.0	2.9	1.8	0.6	1.1

templates if the neutron-star equation of state is not very stiff; i.e., Λ is smaller than ~ 1000 . By contrast, the EOB waveforms may not be yet accurate enough for neutron stars with very stiff equations of state. For TM1, this fact is particularly noticeable: it is clearly found from the result of $\|h_1 - h_2\|$ for the combination of the TM1 EOB and TM1 hybrid waveforms, which differs significantly from zero. This suggests again that, for very stiff equations of state, there is still room for improving the EOB formalism [52].

We also find from Table IV that the values of $\|h_1 - h_2\|$ for the choice of the hybrid-TT4 or TF2 waveforms are appreciably different from those in Table II (except for the APR4 and SFHo equations of state; hybrid-EOB and hybrid-TT4 waveforms agree with each other in a good manner for these equations of state). This fact is also found from, e.g., (i) the diagonal components in Table IV (i.e., for the case that h_1 and h_2 for the same equation of state are employed) differ significantly from zero, particularly for stiff equations of state; (ii) asymmetry between the off-diagonal components, which should be absent for the templates, is appreciable; and (iii) the hybrid-TT4 waveform for the TM1 equation of state matches better with the hybrid (hybrid-EOB) waveform for the TMA than for the TM1. If the hybrid waveforms would be more realistic

ones, these results imply that the hybrid-TT4 and TF2 waveforms would not function as measurement templates as well as the EOB ones. This also indicates that the templates by the TF2 and TT4 approximants would give a systematic bias in the estimation of tidal deformability. This agrees qualitatively with the finding in Ref. [20].

One of the reasons for the disagreement between the two hybrid waveforms (hybrid-EOB and hybrid-TT4) is that the effect of the tidal deformation would be underestimated in the current TT4 approximant, due to the lack of higher-order PN terms (see Sec. III and Appendix B). Another reason is that the matching frequency in our present study ($f \sim 400$ Hz) would still be high. For such a frequency, the EOB and TT4 waveforms do not agree well with each other for high values of Λ and the phase difference is not negligible; for stiff equations of state, the accumulated phase difference is $\sim 0.3(\Lambda/1000)$ rad for $50 \text{ Hz} \leq f \leq 400 \text{ Hz}$ (see Appendix B). The phase difference that results from the incompleteness of the tidal effects would be proportional approximately to Λf_f^α , where $\alpha \geq 8/3$ [see Appendix B and Eqs. (C3) and (C4)] and f_f is the upper end of the matching frequency. Thus, if the hybridization is performed with a lower value of the matching frequency, the disagreement between the two hybrid waveforms would

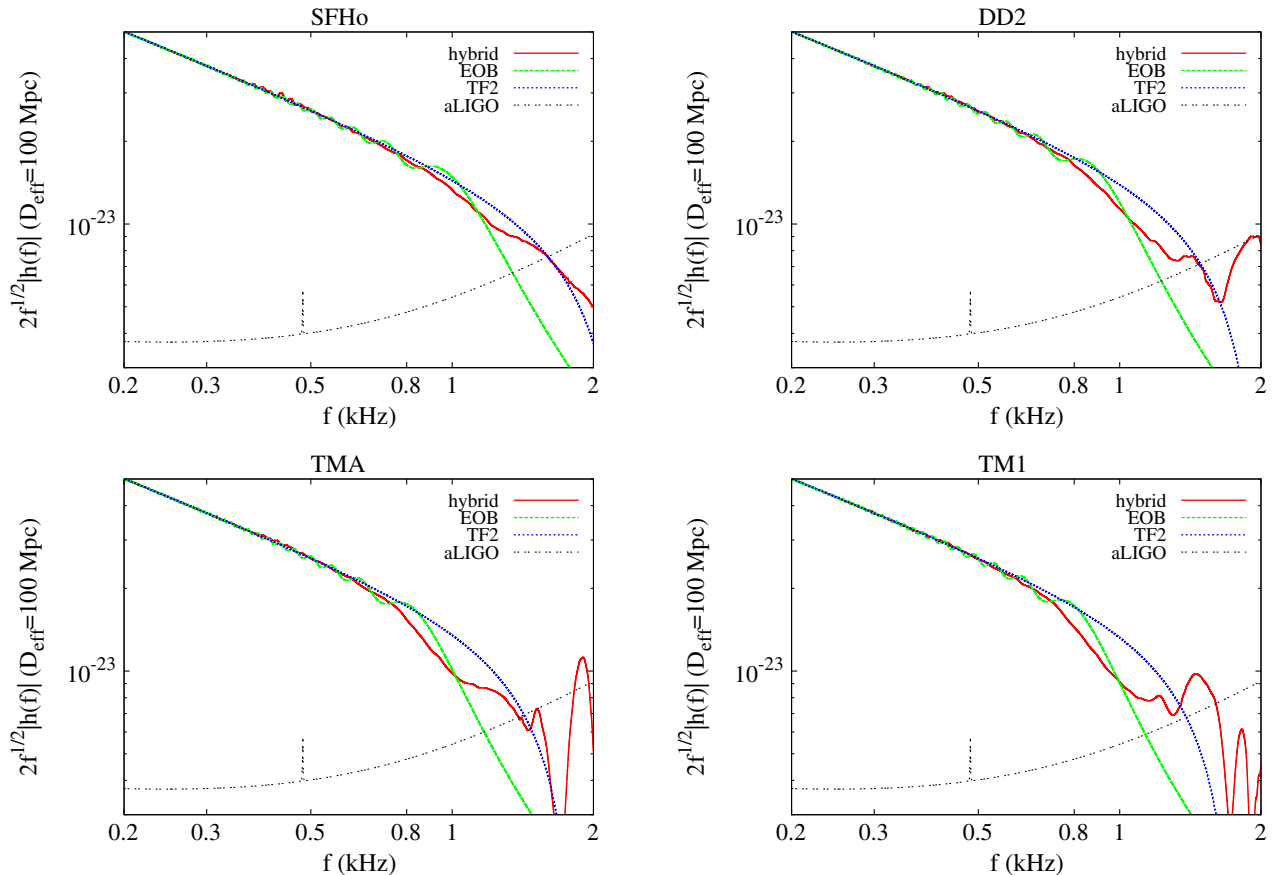


FIG. 5. Comparison of the spectrum shapes of hybrid, Taylor-F2 (TF2), and EOB waveforms for SFHo (upper left panel), DD2 (upper right panel), TMA (lower left panel), and TM1 (lower right panel) equations of state.

be smaller. Our numerical results (compare Figs. 1 and 2) support that the EOB waveforms would be more accurate to perform matching at $f \sim 400$ Hz than the TT4 ones. However, to confirm these speculations, we will have to perform a longer-term simulation and will have to match the waveform at a lower frequency.

One reason that the current version of the TF2 approximant does not reproduce the hybrid waveforms is found from the analysis of the spectrum shape. Figure 5 plots the Fourier spectra of the three different models (hybrid, pure EOB, and TF2) for the SFHo, DD2, TMA, and TM1 equations of state. In the spectrum of the EOB waveform, a modulation is found. This is due to the fact that the time-domain waveform is artificially terminated at the end of the inspiral phase, and hence the spectrum is subject to the Gibbs phenomenon. Besides this modulation, the spectrum shapes of the hybrid and EOB waveforms are in fair agreement for $f \lesssim 1$ kHz. This should be the case because the agreement between the two waveforms has already been found, particularly for the equations of state with $\Lambda < 1000$ (see Fig. 1). By contrast, the spectrum amplitude of the TF2 approximant does not agree well with those of the hybrid waveforms for the late inspiral phase ($f \gtrsim 500$ Hz), in which the tidal effects as well as general relativistic gravity play an important role. The steep decline of the spectrum observed in the hybrid waveforms for $f \gtrsim 500$ Hz cannot be well captured by the current version of the TF2 approximant, particularly for the stiff equations of state like TMA and TM1. This indicates that the tidal effects would not be sufficiently taken into account in this TF2 spectrum amplitude. (We note that this insufficiency is partly due to the use of the stationary phase approximation.)

The phases of the Fourier transform in the hybrid and TF2 waveforms also do not agree well with each other. Figure 6 plots the absolute difference (the upper panel) and phase difference (the lower panel) between the hybrid and

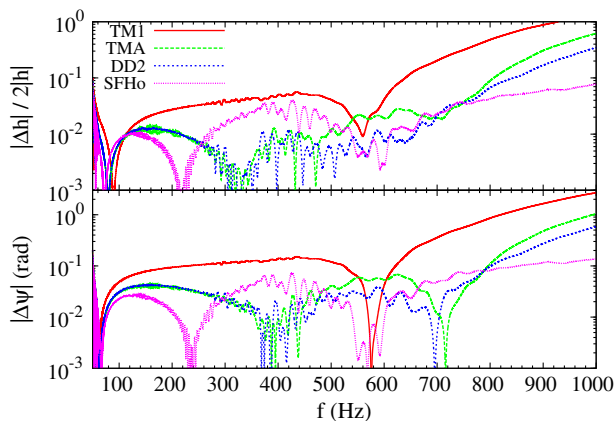


FIG. 6. Absolute values for the difference of the Fourier waveforms (upper panel) and Fourier phases (lower panel) as functions of the gravitational-wave frequency between the hybrid and TF2 waveforms. Note that, at the minima of $\Delta\psi$, its sign changes.

TF2 waveforms for given equations of state. Here, the absolute difference of the waveforms for a given value of f is defined by

$$\frac{|\tilde{h}_1(f) - \tilde{h}_2(f)|}{2|\tilde{h}_1(f)|}, \quad (4.4)$$

where \tilde{h}_1 and \tilde{h}_2 denote the Fourier transform of the hybrid and TF2 waveforms. For plotting Fig. 6, we choose Δt and $\Delta\phi$, which minimize $\|h_1 - h_2\|$ of Eq. (4.1) for $f_i = 50$ Hz and $f_f = 1$ kHz. This figure shows that the absolute difference in the waveform is determined primarily by the phase difference and that the phase difference is generally larger for larger values of Λ . This suggests that the absence of higher-order PN terms in the tidal-deformation effect would be one of the primary sources for the disagreement in the phase.

We also note that the phase difference is present rather uniformly for 50–1000 Hz, even for soft equations of state like SFHo for which the tidal-deformation effect should be minor. This suggests that the absence of not only the tidal effect but also other nontidal higher-order PN terms like 4PN and higher-order terms would cause inaccuracy in the TF2 approximants. A recent study for the extension of the TF2 approximant in the context of binary black holes [61] indeed suggests that the coefficients of the absent higher-order PN terms in phase (ψ_{TF2} : see Appendix C) should be large [the order of α_k with $k \geq 9$ in Eq. (C3) would be of 10^4 or more, i.e., comparable to the tidal-effect terms], perhaps due to the use of the stationary phase approximation, and this should affect the wave phase in the late inspiral stage. Therefore, for improving the performance of the TF2 approximant, we will have to incorporate both the tidal and nontidal higher-order PN terms, which are absent in the current version. We plan to explore this issue in future work.

V. SUMMARY

Combining new gravitational waveforms derived by long-term (14–16 orbits) numerical-relativity simulations with the waveforms by an EOB formalism for coalescing binary neutron stars, we constructed hybrid waveforms and estimated the measurability for the dimensionless tidal deformability of the neutron stars, Λ , by ground-based advanced gravitational-wave detectors, using the hybrid waveforms as the model waveforms. We found that, for an event at a hypothetical effective distance of $D_{\text{eff}} = 200$ Mpc, the distinguishable difference in the dimensionless tidal deformability for $1.35M_{\odot}$ neutron stars will be ≈ 100 , 400, and 800 at 1σ , 2σ , and 3σ levels, respectively, for Advanced LIGO. If the true equation of state is stiff and the corresponding neutron-star radius is $R \gtrsim 13$ km, this suggests that R will be constrained within ≈ 1 km at the 2σ level for an event of $D_{\text{eff}} = 200$ Mpc. On the other hand, if the true equation of state is soft and $R \lesssim 12$ km, it will be difficult to accurately identify the equations of state among many soft candidates,

although it is still possible to discriminate it from stiff equations of state with $R \gtrsim 13$ km. These results indicate that measuring the tidal deformability is a promising method for constraining the neutron-star equation of state in the near future.

The analysis in this paper was carried out for given values of mass and mass ratio of the binaries. In reality, these parameters have to be also determined in the data analysis. The uncertainty in these parameters will enhance the uncertainty in the estimation for the dimensionless tidal deformability, as shown in Ref. [20]. Therefore, the estimation for the measurability of the dimensionless tidal deformability in this paper would be optimistic. We are now deriving more numerical waveforms by changing the mass and mass ratio. A more realistic analysis of the measurability will be carried out in our next work.

We also examined the validity of the waveforms by the EOB, TT4 (hybrid-TT4), and TF2 formalisms. Our analysis shows that these waveforms deviate from our hybrid waveforms. Comparison between the hybrid waveforms and those by these approximants suggests that the EOB waveform would be better than others. However, there is still room for improvement in the current EOB formalism, particularly for neutron stars with stiff equations of state in which $\Lambda > 1000$. For the current version of the TT4 and TF2 approximants, the absence of higher-order PN terms is the likely source for the inaccuracy. For the TT4, the absence of higher-order PN terms in the tidal effects is the main source for the inaccuracy. For the TF2, the absence of both higher-PN terms in the tidal

and nontidal effects is likely to be the source of the inaccuracy. Improving these approximants is one of the interesting issues to be addressed in the future.

ACKNOWLEDGMENTS

We would like to thank the SXS Collaboration for freely providing a variety of high-precision gravitational waveforms of binary-black-hole coalescence. We thank H. Tagoshi and K. Kawaguchi for the helpful discussions. This work was supported by a Grant-in-Aid for Scientific Research (Grant No. 24244028), a Grant-in-Aid for Scientific Research on Innovative Areas “New Developments in Astrophysics Through Multi-Messenger Observations of Gravitational Wave Sources” (Grant No. 15H00782), and a Grant-in-Aid for Research Activity Start-up (Grant No. 15H06857) of Japanese MEXT/JSPS. K. K. was supported by the RIKEN iTHES Project.

APPENDIX A: GRAVITATIONAL-WAVE FREQUENCY EVOLUTION

For providing supplementary information of the gravitational waveforms plotted in Fig. 1, we show gravitational-wave frequency as a function of the retarded time for numerical (solid curves) and EOB (dot-dot curves) waveforms in Fig. 7. As we have already described in Ref. [27], the two frequency curves agree with each other, except for $t_{\text{ret}} \lesssim 5$ ms and for the stage just prior to the merger (around $t_{\text{ret}} \sim 60$ ms). The early-time spike around $t_{\text{ret}} \approx 2$ ms and

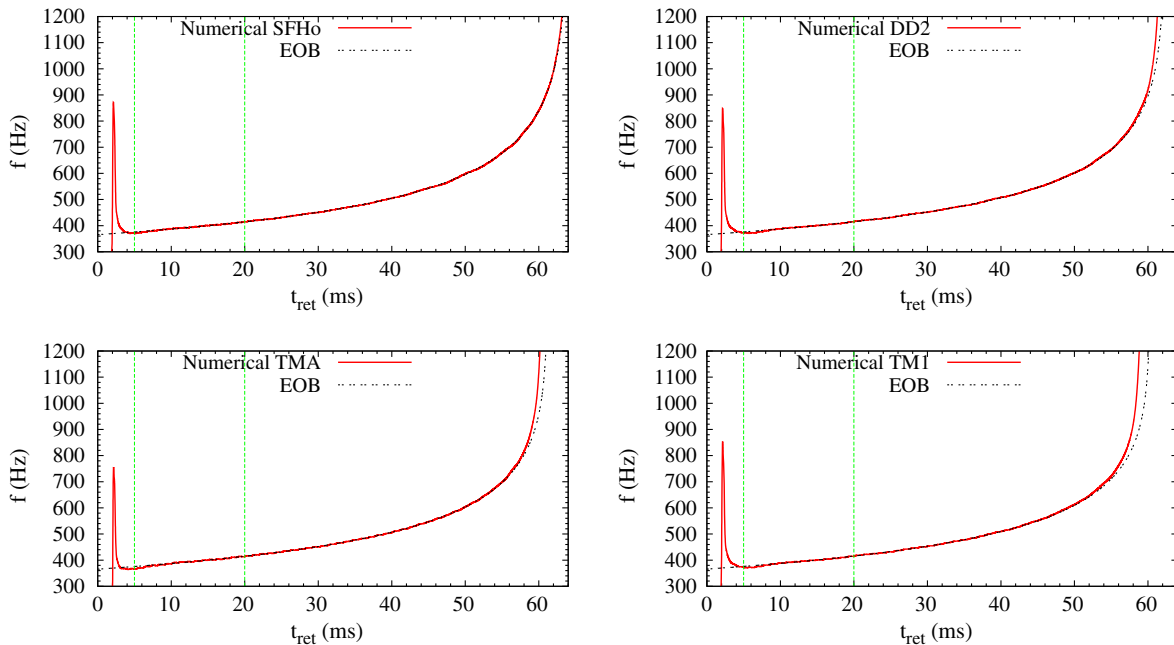


FIG. 7. Gravitational-wave frequency as a function of the retarded time for the SFHo (upper left panel), DD2 (upper right panel), TMA (lower left panel), and TM1 (lower right panel) equations of state. The solid and dot-dot curves denote the results for numerical and EOB waveforms, respectively. The vertical dashed lines show $t_{\text{ret}} = 5$ and 20 ms. The spike at $t_{\text{ret}} \approx 2$ ms is due to the unphysical modulation of the gravitational waveforms (see the text).

the associated modulation are caused by the fact that the initial condition, which describes inspiral binary neutron stars only approximately because a conformal flatness formulation is employed (e.g., Ref. [62]), is contaminated by an unphysical component of gravitational waves. Thus, only the numerical waveforms with $t_{\text{ret}} \gtrsim 5$ ms are reliable. The late-time disagreement is larger for the stiff equation of state which has high values of $\Lambda \gtrsim 1000$, as expected from Fig. 1. This also indicates that there is still room for incorporating additional tidal effects into the EOB formalism to improve it. On the other hand, for softer equations of state with $\Lambda < 1000$, like the SFHo equation of state, the disagreement is minor. This indicates that the EOB waveforms well capture the tidal-deformation effects, as long as $\Lambda \ll 1000$.

APPENDIX B: COMPARISON OF THE EOB AND TT4 WAVE PHASES

We compare the wave phases derived by the EOB and TT4 equations of motion. Figure 8 plots the absolute value of the difference in the wave phases (the wave phase of the TT4 approximant, Φ_{TT4} , minus that of the EOB formalism, Φ_{EOB}) as a function of the gravitational-wave frequency, f , for the APR, SFHo, DD2, TMA, and TM1 equations of state. For taking the difference, we align the two phases at $f = 50$ Hz. For $f \gtrsim 400$ Hz, Φ_{TT4} is always larger than Φ_{EOB} , and the difference steeply increases with f . This is due to the fact that the orbital (gravitational-wave frequency) evolution in the TT4 approximant is slower than that in the EOB formalism in such a frequency band. On the other hand, for $f \lesssim 200$ Hz, Φ_{EOB} is larger by $\lesssim 0.1$ rad than Φ_{TT4} . This would stem from the difference in more than 4PN nontidal terms between the EOB and TT4

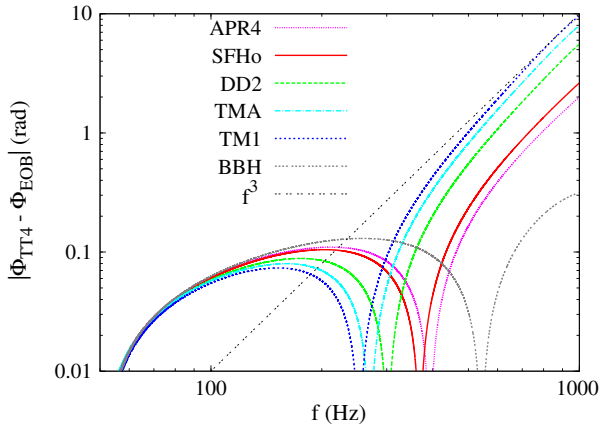


FIG. 8. Absolute value of the difference in the wave phases calculated by the TT4 approximant, Φ_{TT4} , and that of the EOB formalism, Φ_{EOB} , as a function of the gravitational-wave frequency, f . For $f \lesssim 200$ Hz, Φ_{EOB} is always larger than Φ_{TT4} , while for $f \gtrsim 400$ Hz, Φ_{TT4} is always larger than Φ_{EOB} for the binary neutron-star models. The dot-dot line shows $10(f/1 \text{ kHz})^3$ rad. The curve labeled “BBH” is the case for $\Lambda = 0$.

equations of motion. To clarify this fact, we also plot the curve for $\Lambda = 0$ (see the curve labeled “BBH”).

To identify the source of the phase difference in the high-frequency region $f \gtrsim 400$ Hz, we also plot a dot-dot line of $10(f/1 \text{ kHz})^3 \propto x^{9/2}$ in Fig. 8. The slope of this curve approximately captures the behavior of $\Phi_{\text{TT4}} - \Phi_{\text{EOB}}$ for $f \lesssim 1$ kHz. Note that the phase in the TT4 approximant is calculated by

$$\begin{aligned} \Phi_{\text{TT4}} &= 2 \int x^{3/2} \frac{dx}{(dx/dt)} \\ &= \frac{5}{8} \int x^{-7/2} \frac{dx}{F(x)}, \end{aligned} \quad (\text{B1})$$

where the right-hand side of Eq. (3.5) should be substituted for dx/dt and $F(x)$ denotes the terms in $[\cdot \cdot \cdot]$ of Eq. (3.5): $1 - 487x/168 \dots$. Equation (B1) indicates that the error of Φ_{TT4} , which is associated with the insufficiency for incorporating higher-order PN tidal effects, should be of order x^4 for the 1.5PN tidal effect and $x^{9/2}$ for the 2PN tidal effect. The slope of Fig. 8 indicates that the lack of such higher-PN tidal effects would be the dominant source of the disagreement.

Figure 8 shows that the phase difference at $f \approx 400$ Hz is appreciable; it is ~ 0.2 , 0.3 , and 0.4 rad for the DD2, TMA, and TM1 equations of state, respectively. This difference results in disagreement between the hybrid-EOB and hybrid-TT4 waveforms, as illustrated in Sec. III. If the hybridization could be done for a lower-frequency band, the phase difference would be smaller than ~ 0.1 rad and the two hybrid waveforms would agree with each other in a better manner. However, Fig. 8 suggests that the lack of the more than 4PN nontidal terms in the TT4 approximant would also cause the phase disagreement of $O(0.1)$ rad even for $f \lesssim 300$ Hz [if the coefficients of the 4PN terms were of $O(100)$, this would be the case]. This lack of terms could give non-negligible damage for making a measurement template. Higher-order nontidal terms will also be required for improving the TT4 approximant.

APPENDIX C: MEASURABILITY IN THE TAYLOR-F2 APPROXIMANT

By calculating $\|h_1 - h_2\|$ in Eq. (4.1), we also analyzed the measurability of the dimensionless tidal deformability using a TF2 approximant of the inspiraling compact binaries of mass $1.35M_\odot - 1.35M_\odot$. Again, we employ the one-sided noise spectrum density for the zero detuning high power configuration of Advanced LIGO as $S_n(f)$ [56]. Here, for the TF2 approximant, we employ the spinless 3.5PN phasing [54] incorporating the contribution of the tidal deformability up to 1PN order with respect to the leading-order tidal term [14,20]. For the Fourier amplitude, we employ the 3PN formulation for the point-particle approximation, described in Ref. [61], incorporating a tidal correction up to the 1PN order [14,32]. Specifically, the

spectrum is derived from a stationary phase approximation and is assumed to be written in a polynomial form:

$$\tilde{h}_{\text{TF2}}(f) = \frac{m_0^2}{D_{\text{eff}}} \sqrt{\frac{5\pi}{96}} (\pi m_0 f)^{-7/6} e^{i\psi_{\text{TF2}}(f)} A_{\text{TF2}}(f), \quad (\text{C1})$$

where

$$A_{\text{TF2}}(f) = \sum_{k=0}^{12} A_k (\pi m_0 f)^{k/3}, \quad (\text{C2})$$

$$\begin{aligned} \psi_{\text{TF2}}(f) = & 2\pi f t_0 - \phi_0 - \frac{\pi}{4} \\ & + \frac{3}{32} (\pi m_0 f)^{-5/3} \sum_{k=0}^{12} \alpha_k (\pi m_0 f)^{k/3}, \quad (\text{C3}) \end{aligned}$$

and the nonzero components of A_k and α_k in our analysis are

$$A_0 = 1, \quad A_2 = -\frac{37}{48}, \quad A_4 = -\frac{9237931}{2032128},$$

$$A_6 = \frac{41294289857}{7510745088} - \frac{205\pi^2}{192}$$

$$A_{10} = -\frac{27}{16}\Lambda, \quad A_{12} = -\frac{449}{64}\Lambda, \quad (\text{C4})$$

$$\alpha_0 = 1, \quad \alpha_2 = \frac{2435}{378}, \quad \alpha_3 = -16\pi,$$

$$\alpha_4 = \frac{11747195}{254016}, \quad \alpha_5 = \frac{9320}{189}\pi[1 + \ln(\pi m_0 f)],$$

$$\begin{aligned} \alpha_6 = & \frac{1382467552339}{1173553920} - \frac{6848}{21}\gamma_E - \frac{7985\pi^2}{48} \\ & - \frac{6848\gamma_E}{63} \ln(64\pi m_0 f) \end{aligned}$$

$$\alpha_7 = \frac{1428740}{3969}\pi,$$

$$\alpha_{10} = -\frac{39}{2}\Lambda, \quad \alpha_{12} = -\frac{3115}{64}\Lambda. \quad (\text{C5})$$

Here, t_0 is the coalescence time, ϕ_0 is the coalescence phase, γ_E is Euler's constant, and m_0 is the total mass. We restrict our attention only to the formulation in the equal-mass case.

The analysis for the measurability of the tidal deformability was performed by varying f_i and f_f . Six results with different values of f_i and f_f are listed in Table V. Here, we should pay attention only to the results with f_f smaller than ~ 2 kHz because, by the TF2 approximant, the merger and postmerger waveforms are not taken into account. Comparing the results of $(f_i, f_f) = (10, 2000 \text{ Hz})$, $(30, 2000 \text{ Hz})$, $(50, 2000 \text{ Hz})$, and $(100, 2000 \text{ Hz})$, we find that employing $f_i = 30, 50$, and 100 Hz , the values of $\|h_1 - h_2\|$ are systematically underestimated by $\sim 5\%$, 15% , and 30% , respectively.

Comparing the results of $(f_i, f_f) = (10, 500 \text{ Hz})$, $(10, 1000 \text{ Hz})$, and $(10, 2000 \text{ Hz})$, it is found that the values

TABLE V. $\|h_1 - h_2\|$ in a TF2 approximant for a $1.35M_\odot - 1.35M_\odot$ binary at a hypothetical effective distance of $D_{\text{eff}} = 200 \text{ Mpc}$, with several values of f_i and f_f , which are shown in the upper left corner of each table. “ $\Lambda = 0$ ” implies that the dimensionless tidal deformability Λ employed is 0. * denotes the relation of symmetry.

10–500 Hz	$\Lambda = 0$	APR4	SFHo	DD2	TMA	TM1
$\Lambda = 0$...	0.6	0.8	1.6	2.3	2.7
APR4	*	...	0.2	1.0	1.7	2.1
SFHo	*	*	...	0.8	1.5	1.9
DD2	*	*	*	...	0.7	1.1
TMA	*	*	*	*	...	0.5
TM1	*	*	*	*	*	...
10–1000 Hz	$\Lambda = 0$	APR4	SFHo	DD2	TMA	TM1
$\Lambda = 0$...	1.5	1.9	3.2	3.7	4.1
APR4	*	...	0.5	2.3	3.2	3.6
SFHo	*	*	...	1.9	3.0	3.4
DD2	*	*	*	...	1.5	2.4
TMA	*	*	*	*	...	1.1
TM1	*	*	*	*	*	...
10–2000 Hz	$\Lambda = 0$	APR4	SFHo	DD2	TMA	TM1
$\Lambda = 0$...	1.9	2.2	3.3	3.8	4.2
APR4	*	...	0.7	2.5	3.3	3.7
SFHo	*	*	...	2.2	3.0	3.5
DD2	*	*	*	...	1.8	2.5
TMA	*	*	*	*	...	1.3
TM1	*	*	*	*	*	...
30–2000 Hz	$\Lambda = 0$	APR4	SFHo	DD2	TMA	TM1
$\Lambda = 0$...	1.8	2.1	3.1	3.7	4.0
APR4	*	...	0.7	2.4	3.1	3.5
SFHo	*	*	...	2.1	2.9	3.3
DD2	*	*	*	...	1.7	2.4
TMA	*	*	*	*	...	1.3
TM1	*	*	*	*	*	...
50–2000 Hz	$\Lambda = 0$	APR4	SFHo	DD2	TMA	TM1
$\Lambda = 0$...	1.7	2.0	2.9	3.4	3.7
APR4	*	...	0.6	2.2	2.9	3.2
SFHo	*	*	...	1.9	2.7	3.1
DD2	*	*	*	...	1.6	2.2
TMA	*	*	*	*	...	1.2
TM1	*	*	*	*	*	...
100–2000 Hz	$\Lambda = 0$	APR4	SFHo	DD2	TMA	TM1
$\Lambda = 0$...	1.4	1.6	2.4	2.7	3.0
APR4	*	...	0.5	1.8	2.3	2.6
SFHo	*	*	...	1.6	2.2	2.5
DD2	*	*	*	...	1.3	1.8
TMA	*	*	*	*	...	0.9
TM1	*	*	*	*	*	...

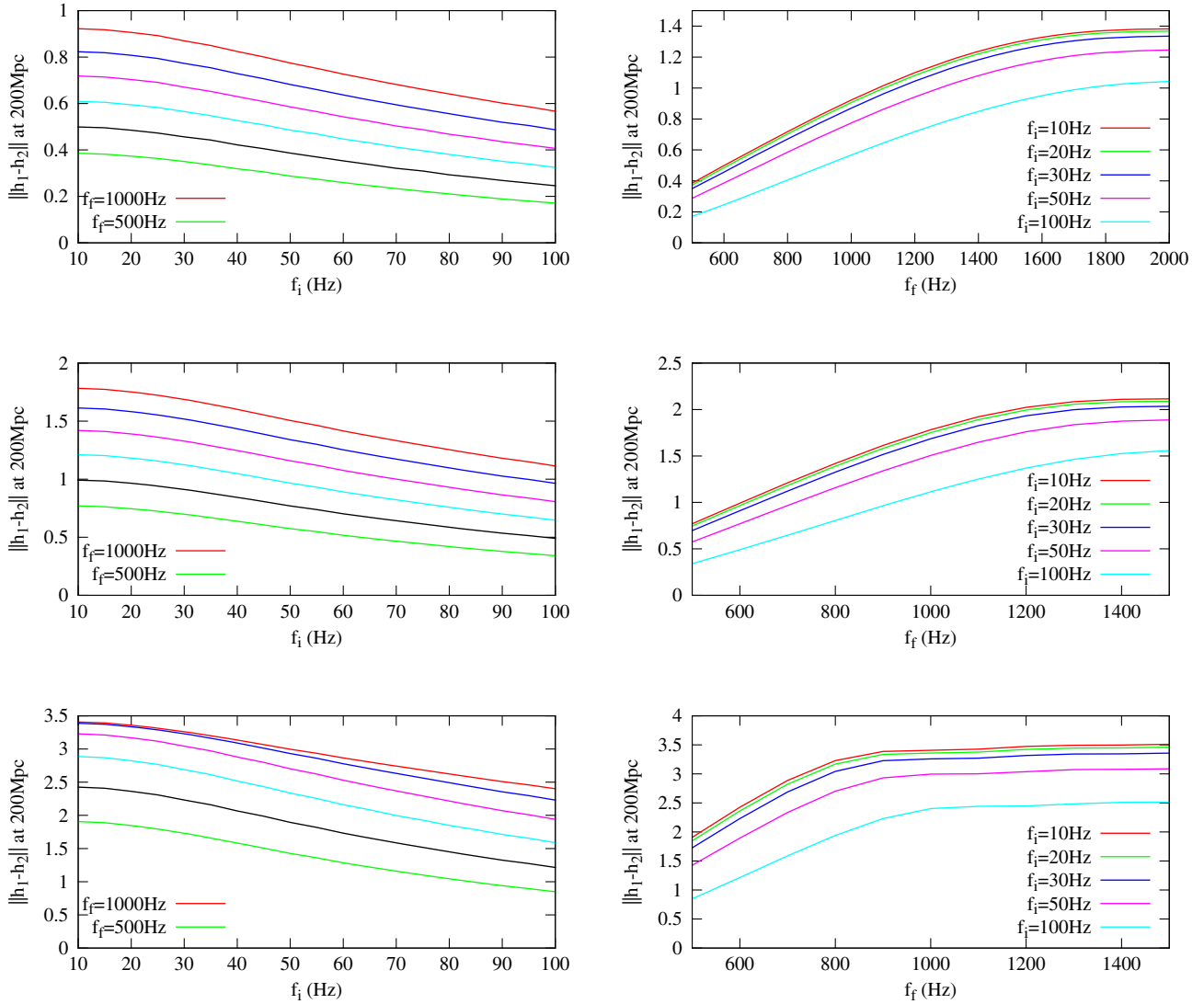


FIG. 9. (Left panels) $\|h_1 - h_2\|$ as a function of f_i for $f_f = 500 - 1000$ Hz, with $\delta\Lambda = 200$ (top panels), 400 (middle panels), and 1000 (bottom panels), respectively. In each panel, the results for $f_f = 500, 600, 700, 800, 900,$ and 1000 Hz are plotted (from the bottom to the top curves). (Right panels) $\|h_1 - h_2\|$ as a function of f_f for $f_i = 10 - 100$ Hz, with $\delta\Lambda = 200$ (top panels), 400 (middle panels), and 1000 (bottom panels), respectively.

of $\|h_1 - h_2\|$ are underestimated by a factor of 2 for $f_f = 500$ Hz. This is reasonable because the tidal-deformation effect in the phasing is accumulated most significantly in the final-inspiral orbits. The values of $\|h_1 - h_2\|$ for (10,1000 Hz) are only smaller by ≤ 0.2 than those for (10,2000 Hz) for the case that $\|h_1 - h_2\| \geq 2.5$. On the other hand, for $\|h_1 - h_2\| \lesssim 2$, the difference between the two cases can be 0.3–0.4. For such a case, it would be necessary to choose $f_f > 1$ kHz.

To further describe the dependence of $\|h_1 - h_2\|$ on the choice of f_i and f_f , we generate Fig. 9. In the left three panels of Fig. 9, we plot $\|h_1 - h_2\|$ at $D_{\text{eff}} = 200$ Mpc as a function of f_i for $f_f = 500 - 1000$ Hz, with $(\Lambda_1, \Lambda_2) = (200, 0)$ (the top panel), $(400, 0)$ (the middle panel), and $(1000, 0)$ (the bottom panel) (referred to as $\delta\Lambda = 200, 400,$

and 1000), respectively. In the three right panels of Fig. 9, we plot $\|h_1 - h_2\|$ at $D_{\text{eff}} = 200$ Mpc as a function of f_f for $f_i = 10 - 100$ Hz, with $\delta\Lambda = 200$ (top panels), 400 (middle panels), and 1000 (bottom panels), respectively. As the left panels of this figure indicate, the values of $\|h_1 - h_2\|$ for $f_i = 30$ and 50 Hz are smaller by $\approx 5\%$ and 15% , respectively, than those for $f_i = 10$ Hz, irrespective of $\delta\Lambda$, for which we choose a realistic range. This suggests that, for $\|h_1 - h_2\| \lesssim 4$, the values of $\|h_1 - h_2\|$ are underestimated only for a small fraction within 0.2 and 0.6, respectively, if we choose $f_i = 30$ and 50 Hz. Such a fraction (particularly for $f_i = 30$ Hz) does not change our conclusion in this paper. As the right panels indicate, this property is independent of the choice of f_f .

The three right panels of Fig. 9 show that, for a large value of $\delta\Lambda \gtrsim 400$, $\|h_1 - h_2\|$ depends only weakly on the choice of f_f as long as it is larger than ≈ 1.5 kHz. For $\delta\Lambda = 200$, $\|h_1 - h_2\|$ appears to increase with f_f , even at $f_f = 1.5$ kHz. The reason for this is that, for a small value

of $\delta\Lambda$, the value of $\|h_1 - h_2\|$ is accumulated relatively in a higher frequency range. Thus, for such a case, it is necessary to take a high value of $f_f \sim 2$ kHz: approximately the highest frequency of gravitational waves prior to the merger.

-
- [1] J. Abadie *et al.* (LIGO Scientific Collaboration), *Nucl. Instrum. Methods Phys. Res., Sect. A* **624**, 223 (2010); T. Accadia *et al.* (Virgo Collaboration), *Classical Quantum Gravity* **28**, 025005 (2011); **28**, 079501(E) (2011); K. Kuroda (LCGT Collaboration), *Classical Quantum Gravity* **27**, 084004 (2010).
- [2] Advanced LIGO, <http://www.advancedligo.mit.edu/>.
- [3] Advanced VIRGO, <http://www.cascina.virgo.infn.it/advirgo/>.
- [4] KAGRA, <http://gwcenter.icrr.u-tokyo.ac.jp/en/>.
- [5] B. P. Abbott *et al.*, *Phys. Rev. Lett.* **116**, 061102 (2016).
- [6] V. Kalogera, K. Belczynski, C. Kim, R. Oshaughnessy, and B. Willems, *Phys. Rep.* **442**, 75 (2007).
- [7] J. Abadie *et al.* (LIGO Scientific and Virgo Collaborations), *Classical Quantum Gravity* **27**, 173001 (2010).
- [8] C. Kim, B. B. P. Perera, and M. A. McLaughlin, *Mon. Not. R. Astron. Soc.* **448**, 928 (2015).
- [9] J. M. Lattimer, *Annu. Rev. Nucl. Part. Sci.* **62**, 485 (2012).
- [10] D. Lai, F. A. Rasio, and S. L. Shapiro, *Astrophys. J.* **420**, 811 (1994).
- [11] T. Mora and C. M. Will, *Phys. Rev. D* **69**, 104021 (2004).
- [12] E. E. Flanagan and T. Hinderer, *Phys. Rev. D* **77**, 021502(R) (2008).
- [13] T. Hinderer, B. D. Lackey, R. N. Lang, and J. S. Read, *Phys. Rev. D* **81**, 123016 (2010).
- [14] J. Vines, E. E. Flanagan, and T. Hinderer, *Phys. Rev. D* **83**, 084051 (2011).
- [15] D. Bini, T. Damour, and G. Faye, *Phys. Rev. D* **85**, 124034 (2012).
- [16] J. S. Read, L. Baiotti, J. D. E. Creighton, J. L. Friedman, B. Giacomazzo, K. Kyutoku, C. Markakis, L. Rezzolla, M. Shibata, and K. Taniguchi, *Phys. Rev. D* **88**, 044042 (2013).
- [17] W. Del Pozzo, T. G. F. Li, M. Agathos, C. Van Den Broeck, and S. Vitale, *Phys. Rev. Lett.* **111**, 071101 (2013).
- [18] M. Favata, *Phys. Rev. Lett.* **112**, 101101 (2014).
- [19] K. Yagi and N. Yunes, *Phys. Rev. D* **89**, 021303 (2014).
- [20] L. Wade, J. D. E. Creighton, E. Ochsner, B. D. Lackey, B. F. Farr, T. B. Littenberg, and V. Raymond, *Phys. Rev. D* **89**, 103012 (2014).
- [21] M. Agathos, J. Meidam, W. Del Pozzo, T. G. F. Li, M. Tompitak, J. Veitch, S. Vitale, and C. Van Den Broeck, *Phys. Rev. D* **92**, 023012 (2015).
- [22] M. Thierfelder, S. Bernuzzi, and B. Brügmann, *Phys. Rev. D* **84**, 044012 (2011).
- [23] S. Bernuzzi, M. Thierfelder, and B. Brügmann, *Phys. Rev. D* **85**, 104030 (2012).
- [24] S. Bernuzzi, A. Nagar, M. Thierfelder, and B. Brügmann, *Phys. Rev. D* **86**, 044030 (2012).
- [25] K. Hotokezaka, K. Kyutoku, and M. Shibata, *Phys. Rev. D* **87**, 044001 (2013).
- [26] D. Radice, L. Rezzolla, and F. Galeazzi, *Mon. Not. R. Astron. Soc.* **437**, L46 (2014).
- [27] K. Hotokezaka, K. Kyutoku, H. Okawa, and M. Shibata, *Phys. Rev. D* **91**, 064060 (2015).
- [28] S. Bernuzzi, A. Nagar, T. Dietrich, and T. Damour, *Phys. Rev. Lett.* **114**, 161103 (2015).
- [29] S. Bernuzzi, T. Dietrich, and A. Nagar, *Phys. Rev. Lett.* **115**, 091101 (2015).
- [30] K. Barkett, M. A. Scheel, R. Haas, C. D. Ott, S. Bernuzzi, D. A. Brown, B. Szilágyi, J. D. Kaplan, J. Lippuner, C. D. Muhlberger, F. Foucart, and M. D. Duez, *Phys. Rev. D* **93**, 044064 (2016).
- [31] T. Damour and A. Nagar, *Phys. Rev. D* **81**, 084016 (2010).
- [32] T. Damour, A. Nagar, and L. Villain, *Phys. Rev. D* **85**, 123007 (2012).
- [33] T. Damour, A. Nagar, and S. Bernuzzi, *Phys. Rev. D* **87**, 084035 (2013); the code is available at <https://eob-new.ihep.fr>.
- [34] D. Bini and T. Damour, *Phys. Rev. D* **87**, 121501(R) (2013).
- [35] D. Bini and T. Damour, *Phys. Rev. D* **90**, 124037 (2014).
- [36] K. Kyutoku, M. Shibata, and K. Taniguchi, *Phys. Rev. D* **90**, 064006 (2014).
- [37] T. Yamamoto, M. Shibata, and K. Taniguchi, *Phys. Rev. D* **78**, 064054 (2008).
- [38] M. Shibata and T. Nakamura, *Phys. Rev. D* **52**, 5428 (1995); T. W. Baumgarte and S. L. Shapiro, *Phys. Rev. D* **59**, 024007 (1998); M. Campanelli, C. O. Lousto, P. Marronetti, and Y. Zlochower, *Phys. Rev. Lett.* **96**, 111101 (2006); J. G. Baker, J. Centrella, D.-I. Choi, M. Koppitz, and J. van Meter, *Phys. Rev. Lett.* **96**, 111102 (2006).
- [39] D. Hilditch, S. Bernuzzi, M. Thierfelder, Z. Cao, W. Tichy, and B. Brügmann, *Phys. Rev. D* **88**, 084057 (2013).
- [40] LORENE Web page: <http://www.lorene.obspm.fr/>.
- [41] A. Steiner, M. Hempel, and T. Fischer, *Astrophys. J.* **774**, 17 (2013).
- [42] S. Banik, M. Hempel, and D. Bandyopadhyay, *Astrophys. J. Suppl. Ser.* **214**, 22 (2014).
- [43] M. Hempel, T. Fischer, J. Schaffner-Bielich, and M. Liebendörfer, *Astrophys. J.* **748**, 70 (2012).
- [44] H. Shen, H. Toki, K. Oyamatsu, and K. Sumiyoshi, *Nucl. Phys. A* **637**, 435 (1998).
- [45] P. B. Demorest, T. Pennucci, S. M. Ransom, M. S. E. Roberts, and J. W. T. Hessels, *Nature (London)* **467**, 1081 (2010); J. Antoniadis *et al.*, *Science* **340**, 123232 (2013).

- [46] A. Akmal, V. R. Pandharipande, and D. G. Ravenhall, *Phys. Rev. C* **58**, 1804 (1998).
- [47] K. Hotokezaka, K. Kiuchi, K. Kyutoku, T. Muranushi, Y.-I. Sekiguchi, M. Shibata, and K. Taniguchi, *Phys. Rev. D* **88**, 044026 (2013).
- [48] C. Reisswig and D. Pollney, *Classical Quantum Gravity* **28**, 195015 (2011).
- [49] C. O. Lousto, H. Nakano, Y. Zlochower, and M. Campanelli, *Phys. Rev. D* **82**, 104057 (2010).
- [50] H. Nakano, *Classical Quantum Gravity* **32**, 177002 (2015).
- [51] B. D. Lackey, K. Kyutoku, M. Shibata, P. R. Brady, and J. L. Friedman, *Phys. Rev. D* **89**, 043009 (2014).
- [52] However, see T. Hinderer *et al.*, [arXiv:1602.00599](https://arxiv.org/abs/1602.00599).
- [53] M. Boyle, D. A. Brown, L. E. Kidder, A. H. Mroué, H. P. Pfeiffer, M. A. Scheel, G. B. Cook, and S. A. Teukolsky, *Phys. Rev. D* **76**, 124038 (2007).
- [54] P. Ajith *et al.*, [arXiv:0709.0093](https://arxiv.org/abs/0709.0093).
- [55] M. Boyle, A. Buonanno, L. E. Kidder, A. H. Mroué, Y. Pan, H. P. Pfeiffer, and M. A. Scheel, *Phys. Rev. D* **78**, 104020 (2008).
- [56] See <https://dcc.ligo.org/cgi-bin/DocDB/ShowDocument?docid=2974>.
- [57] See <https://www.black-holes.org/waveforms/>.
- [58] J. Abadie *et al.*, *Classical Quantum Gravity* **27**, 173001 (2010); C. Kim, B. B. P. Perena, and M. A. McLaughlin, *Mon. Not. R. Astron. Soc.* **448**, 928 (2015).
- [59] J. Clark, A. Bauswein, L. Cadonati, H.-Th. Janka, C. Pankow, and N. Stergioulas, *Phys. Rev. D* **90**, 062004 (2014).
- [60] L. Lindblom, B. J. Owen, and D. A. Brown, *Phys. Rev. D* **78**, 124020 (2008).
- [61] S. Khan, S. Husa, M. Hannam, F. Ohme, M. Pürrer, X. J. Forteza, and A. Bohé, *Phys. Rev. D* **93**, 044007 (2016).
- [62] K. Taniguchi and M. Shibata, *Astrophys. J. Suppl. Ser.* **188**, 187 (2010).